



**Aalto University**  
**School of Chemical**  
**Engineering**



**TECHNISCHE**  
**UNIVERSITÄT**  
**WIEN**  
Vienna University of Technology

# Master thesis

## Heat transfer modeling of a thin film evaporator in ionic liquid purification

carried out for the purpose of obtaining the degree of  
Master of Science (MSc or Dipl.-Ing. or DI)

under the supervision of

**Prof. Ville Alopaeus**

and

**Ass.Prof. Dipl.-Ing. Dr. Michael Harasek**

E166

Institute of Chemical, Environmental & Biological Engineering

submitted at TU Wien,

**Faculty of Mechanical and Industrial Engineering**

**Max Zrunek**

Matrikelnummer 1127921

Obkirchgasse 1/6 1190 Wien



I confirm that going to press this thesis needs the confirmation of the examination committee.

## Affidavit

I declare in lieu of oath, that I wrote this thesis and performed the associated research myself, using only literature cited in this volume. If text passages from sources are used literally, they are marked as such. I confirm that this work is original and has not been submitted elsewhere for any examination, nor currently under consideration for a thesis elsewhere.

Vienna, September, 2017

---

Max Zrunek

# Abstract

In this work the heat transfer of a thin-film evaporator in ionic liquid purification, as a recycling step in a cellulose fiber production process, was modeled.

A literature survey over the field of falling film and agitated thin film evaporation was undertaken to summarize the existing knowledge on the process. To provide a basic understanding of the model dynamics, a short introduction over the area of computational fluid dynamics was given also. A brief enumeration of exemplary research CFD applications of evaporation processes rounded off the theoretical part.

Experiments with the thin-film evaporation were conducted to evaluate the process parameters and to create an empirical basis for the model evaluation. In a first stage, a correlation analysis of the different process variables was completed with the results of the thin-film evaporation of water. Then, in the second stage the process parameters were adjusted for a conclusive set of experiments for ionic-liquid purification that represented the actual experimental basis for the model evaluation.

The modeling part consists of three different models. In the first one, a two-phase CFD Openfoam model was used to set up a case for falling-film flow. Although it was not possible to build up a fully working model, it provided some information on the validity of previous assumptions of thin film evaporation. Two other models were designed in Comsol to predict the heat transfer of the process in terms of required vaporization energy for evaporation. Both were liquid single-phase models. Instead of a continuous flow a series of ideal stages was assumed. Each single stage was simulated in the model and the results were interpolated to attain a result over the whole evaporator column.

The models were opposed to the experimental values. In three out of four cases the model did not match with the empirical result. The possible reasons for the divergence were discussed and summarized.

# Kurzfassung

In dieser Arbeit wurde der Wärmeübergang eines Dünnschichtverdampfers im Zuge eines Wiederaufbereitungsschrittes ionischer Flüssigkeit innerhalb eines Zellulosefaserprozesses modelliert.

Eine Literaturrecherche über Dünnschicht- und Freifallverdampfer wurde durchgeführt, um den aktuellen Stand der Technik zusammenzufassen. Als eine kurze Einleitung in die Modellierung dieser Verfahren wurde ein kurzer Überblick über die numerische Strömungssimulation, CFD, gegeben. Weiters wurden einige repräsentative Anwendungsfälle aufgelistet.

Im Zuge der Arbeit wurden experimentelle Versuchreihen an einem Labor Dünnschichtverdampfer durchgeführt. In einem ersten Schritt wurde ein Parameter-Screening und eine Korrelationsanalyse durchgeführt. In einem zweiten Schritt wurde ein angepasstes Set an Parametern herangezogen, um eine Versuchsreihe als Grundlage zur Modellvalidierung zu erhalten.

Der Modellierungsteil besteht aus drei verschiedenen Modellen. Das erste Modell wurde in Openfoam mit einem Zweiphasensolver erstellt. Die Ergebnisse gaben Auskunft über die Gültigkeit angenommener Randbedingungen vorangegangener Arbeiten. Zwei weitere Modelle wurden in COMSOL programmiert. Als limitierender Faktor für die auftretende Verdampfung wurde die konstant angenommene spezifische Verdampfungsenthalpie bestimmt. Mithilfe Energiebilanzen wurden Wärmeübergangskoeffizienten sowohl über die Modelle geschätzt als auch experimentell bestimmt. Der so ermittelte Wärmeübergangskoeffizient wurde für das dritte Modell festgelegt. Im dritten Modell wurde der gesamte Verdampfer als eine Kolonne idealer Trennstufen abgebildet. Für jede dieser Trennstufen wurde in einer definierten Modellgeometrie der resultierende Wärmestrom und verdampfende Massenstrom berechnet.

Die Modellergebnisse wurden experimentellen Resultaten gegenübergestellt. In drei von vier Fällen stimmten die experimentellen Ergebnisse mit den Modellprognosen nicht überein. Mögliche Ursachen der Abweichung wurden diskutiert und zusammengefasst.

# Acknowledgements

When I graduated from my A-levels, the chairman of the examination board made an appeal to the tax payer's contribution. Back then, I broke out laughing after his speech as I was surprised by his thoughts to thank public community so unexpectedly and not acknowledge the performance of the students first.

Now, eight years later I slowly understand what he meant. Having been six years at university, I must say that I have had a delightful time from a personal and educational point of view. I don't know, if I had started at university immediately, if the circumstances had been different. Anyhow, I did it for two major reasons: I preferred studying over working as it was free and nonetheless the given financial support from my family. At this point I want to thank my parents, Marja and Ulrich, and my grandfather Reijo to take care of my expenditures.

I chose to study chemical engineering as I developed a certain genuine interest for chemistry due to the good tuition of my chemistry teachers in high school, Isabella Stadler and Manfred Kerschbaumer.

During my time at the Technical University of Vienna I had some challenging exams to pass that I deemed to be unnecessary ordeals, but my fellow students always supported me in those tough situations. Besides, we had a great time off the campus too.

The leading characters for this work however, were my supervisors in Finland, Kaj Jacobsson and Ville Alopaeus. I value their calm approach towards the questions that I faced in my thesis and the very relaxed, straightforward communication during our discussions. Furthermore, I would like to thank Armelle Garcia for supporting me on the experimental part of the thesis, especially for the experiments with ionic liquid water separation, which she carried out on her own.

From Vienna's side I'd like to thank Michael Harasek as my Austrian supervisor for the handling of the administrative work in Vienna.

And at last, but not at least, I want to express my gratitude towards my siblings, my

sisters Kirsti and Satu and my brother Axel-Michael.

Thank you all very much!

# List of Figures

1.1	Falling film evaporator . . . . .	3
1.2	Agitated thin film evaporator . . . . .	4
1.3	Temperature profiles falling film . . . . .	5
1.4	Boiling curve . . . . .	11
1.5	Phase transition . . . . .	12
1.6	Billet's theory . . . . .	16
1.7	Gropp and Schlünder theory . . . . .	16
2.1	Grid of finite volumes . . . . .	24
2.2	Upwind scheme . . . . .	25
2.3	Smoothing of discontinuous functions . . . . .	30
2.4	Element types FEM . . . . .	31
2.5	Structure OF . . . . .	33
2.6	GUI Comsol . . . . .	33
3.1	PI diagram . . . . .	37
3.2	Confidence band water evaporation . . . . .	42
3.3	Fluctuation range of IL experiments . . . . .	49
4.1	Openfoam case geometry . . . . .	55
4.2	Principle of an ideal stage thin-film evaporation . . . . .	58
4.3	principle of falling film with co-current gas flow . . . . .	58
4.4	Evaporator model geometry . . . . .	60
4.5	Model sections . . . . .	60
4.6	Grid refinement 5 . . . . .	61



4.7	Grid refinement 45 . . . . .	61
4.8	Deviation of $w$ along $\delta_f^+$ . . . . .	62
4.9	Experiment heat transfer coefficients at different temperatures . . . . .	65
4.10	Boiling curves Aspen Plus . . . . .	69
4.11	Total theoretical height E1 . . . . .	72
4.12	Total theoretical height E4 . . . . .	72
4.13	Process parameters as functions of $x_1$ . . . . .	73
4.14	Counter current heat exchanger . . . . .	77
6.1	Appendix PID flowsheet II . . . . .	95
6.2	Appendix thin-film evaporator drawing . . . . .	96
6.3	T-x,y phase diagram of the [DBNH][OAc]-H <sub>2</sub> O binary (Aspenplus, UNIQUAC)	97

# List of Tables

1.1	Coefficients Nusselt correlation . . . . .	5
1.2	Gibbs phase rule evaporation cases . . . . .	9
2.1	general terms in the governing equations . . . . .	21
2.2	Different weighted residual methods . . . . .	23
2.3	Element types FEM . . . . .	32
3.1	Experimental matrix water evaporation . . . . .	39
3.2	Fluctuation range water evaporation . . . . .	40
3.3	Experimental results water evaporation . . . . .	41
3.4	$\frac{c_p \Delta T^*}{h_{vap}}$ ratio . . . . .	43
3.5	Correlation matrix water evaporation . . . . .	44
3.6	Residue temperature vs. saturation temperature water . . . . .	45
3.7	Experimental heat transfer coefficients water evaporation . . . . .	45
3.8	Experimental Settings ionic liquid purification . . . . .	47
3.9	Experimental results ionic liquid purification . . . . .	48
3.10	Fluctuation range IL experiments . . . . .	48
3.11	Experimental heat transfer coefficients IL . . . . .	49
3.12	Comparison experiments . . . . .	50
4.1	Boundary conditions of the OpenFoam case . . . . .	56
4.2	Deviations for different $n_{grid}$ . . . . .	62
4.3	Experimental heat transfer coefficient water evaporation . . . . .	64
4.4	Boundary conditions IL model . . . . .	66
4.5	Process parameter IL model . . . . .	67

*List of Tables*

4.6	Material parameters IL model . . . . .	68
4.7	discrete modeled values E1 . . . . .	71
4.8	Modeled theoretical lengths . . . . .	72
4.9	Modeled and experimental heat flux . . . . .	73
4.10	Thermal resistance wall . . . . .	74
4.11	Thermal resistance film . . . . .	75
4.12	Required surface area model . . . . .	76
4.13	Logarithmic temperature difference model . . . . .	78
4.14	Distillate heating jacket temperature model . . . . .	78
4.15	Logarithmic temperature difference experimental values . . . . .	79
6.1	Geometry dimensions of the thin-film evaporator . . . . .	96
6.2	Discrete model values E1 . . . . .	98
6.3	Discrete model values E2 . . . . .	99
6.4	Discrete model values E3 . . . . .	100
6.5	Discrete model values E4 . . . . .	101
6.6	Overview of different IL experiments . . . . .	102
6.7	Experimental values of the residue temperature for different run times . . . . .	102

# Nomenclature

## Vectors and tensors

$a$	scalar	
$\mathbf{a}$	vector, tensor	
$\mathbf{A}$	Matrix	
$\dot{\mathbf{q}}$	heat flux vector	$\frac{W}{m^2}$
$\mathbf{u} = (u, v, w)^t$	velocity vector	$\frac{m}{s}$
$\mathbf{x} = (x, y, z)^t$	position vector	$m$
$\boldsymbol{\tau}$	shear stress tensor	$Pa$

## Latin characters

$A$	area	$m^2$
$c$	concentration	$\frac{mol}{m^3}$
$c_p$	specific heat capacity	$\frac{J}{kg \cdot K}$
$d$	diameter	$m$
$g$	gravitational constant	$\frac{m}{s^2}$
$h$	specific enthalpy	$\frac{J}{kg}$
$p$	pressure	$Pa$
$s$	standard deviation	
$T$	thermodynamic temperature	$K$
$x$	liquid mass fraction <sup>1</sup>	
$x_m$	liquid molar fraction <sup>1</sup>	
$\dot{M}$	mass flow rate	$\frac{kg}{s}$
$\dot{m}$	mass flux	$\frac{kg}{m^2 \cdot s}$
$\dot{Q}$	heat rate	$W$
$\dot{q}$	heat flux	$\frac{W}{m^2}$
$\dot{V}$	volumetric flow rate	$\frac{m^3}{s}$

---

<sup>1</sup>relates to the compound composition. For example the *mass* of the more volatile component in relation to the distillate compound:  $x_{1,d} = \frac{m_{1,d}}{m_d}$ . For the molar fraction the component *amount* is used instead

## Greek characters

$\alpha$	heat transfer coefficient	$\frac{W}{m^2 K}$
$\delta_l$	falling film thickness	$\frac{m}{s^2}$
$\lambda$	heat conductivity	$\frac{W}{m \cdot K}$
$\mu$	kinematic viscosity	$Pa s$
$\nu$	dynamic viscosity	$\frac{m}{s^2}$
$\varphi$	interpolation function	
$\rho$	density	$\frac{kg}{m^3}$
$\sigma$	surface tension	$\frac{N}{m}$
$\theta$	temperature	$^{\circ}C$
$\zeta$	feed mass fraction <sup>2</sup>	

## Sub- and superscripts

$a_l$	liquid
$a_g$	gaseous
$a_e$	evaporator
$a_i$	component
$a_w$	wall
$a_e$	element
$a_f$	film
$a_m$	molar
$a_{sat}$	saturation point
$a_F$	feed
$a_R$	residue

---

<sup>2</sup>the ratio between one compound and the feed. For example the distillate mass fraction  $\zeta_d = \frac{m_d}{m_F}$

## Dimensionless numbers

$Ka$	Kaptiza number
$Nu$	Nusselt number
$Pr$	Prandtl number
$Re$	Reynolds number
$Sc$	Schmidt number
$Sh$	Sherwood number

## Operators

$\nabla \mathbf{a}$	gradient
$\nabla \cdot \mathbf{a}$	divergence
$\frac{D}{Dt}$	Material derivative
$\frac{d}{dt}$	total derivative
$\frac{\partial}{\partial t}$	partial derivative

## Abbreviations

<b>CFD</b>	Computational fluid dynamics
<b>FVM</b>	Finite volume method
<b>FEM</b>	Finite element method
<b>VoF</b>	Volume of fluid
<b>IL</b>	Ionic liquid
<b>OF</b>	OpenFOAM
<b>[DBNH][OAc]</b>	1,5-diazabicyclo[4.3.0]non-5-enium acetate

# Contents

<b>1</b>	<b>Introduction</b>	<b>1</b>
1.1	Background . . . . .	1
1.2	Evaporators . . . . .	2
1.2.1	Falling film evaporators . . . . .	2
1.2.2	Wiped film evaporators . . . . .	3
1.3	Heat transfer . . . . .	4
1.3.1	Falling film flow . . . . .	4
1.3.2	Energy balance . . . . .	6
1.3.3	Evaporation . . . . .	8
1.3.4	Wiped film evaporators . . . . .	12
1.4	Mass transfer . . . . .	14
1.4.1	Falling film . . . . .	14
1.4.2	Wiped film . . . . .	15
<b>2</b>	<b>Computational fluid dynamics</b>	<b>19</b>
2.1	Governing equations . . . . .	19
2.1.1	Reynolds transport theorem . . . . .	20
2.1.2	Conservation laws . . . . .	20
2.2	Numerical computation . . . . .	21
2.2.1	Discretization . . . . .	21
2.2.2	Weighted residual methods . . . . .	22
2.3	Finite volume method . . . . .	23
2.3.1	Control volume . . . . .	23
2.3.2	Interpolation . . . . .	24



## Contents

2.4	Finite element method . . . . .	27
2.4.1	General approach . . . . .	28
2.4.2	Weighted residual methods - weak formulation . . . . .	29
2.4.3	Elements . . . . .	31
2.5	CFD applications . . . . .	32
2.5.1	Introduction to Openfoam . . . . .	32
2.5.2	Introduction to Comsol . . . . .	33
2.5.3	CFD modeling in evaporation processes . . . . .	34
<b>3</b>	<b>Experiments</b>	<b>37</b>
3.1	Set-up . . . . .	37
3.2	Water evaporation . . . . .	38
3.2.1	Water evaporation results . . . . .	39
3.2.2	Conclusions . . . . .	46
3.3	Ionic liquid separation . . . . .	46
3.3.1	Results ionic liquid separation . . . . .	47
3.3.2	Heat transfer coefficient . . . . .	48
3.3.3	Previous experiments . . . . .	49
3.3.4	Conclusions . . . . .	50
<b>4</b>	<b>Models</b>	<b>53</b>
4.1	$OF_{H_2O}$ model . . . . .	54
4.2	$COM_{H_2O}$ model . . . . .	57
4.2.1	Analytical Solution . . . . .	58
4.2.2	Geometry . . . . .	59
4.2.3	Grid independence study . . . . .	61
4.2.4	Modules and boundary conditions . . . . .	63
4.2.5	Determination of the heat transfer coefficient . . . . .	63
4.3	$COM_{IL/H_2O}$ model . . . . .	65
4.3.1	Geometry . . . . .	66

4.3.2	Modules and boundary conditions . . . . .	66
4.3.3	Parameters . . . . .	67
4.3.4	Boiling curve diagram . . . . .	69
4.3.5	Results of the $COM_{IL/H_2O}$ model . . . . .	70
4.3.6	Assessment calculations . . . . .	75
4.4	Conclusions . . . . .	79
<b>5</b>	<b>Outlook</b>	<b>83</b>
	<b>Bibliography</b>	<b>87</b>
<b>6</b>	<b>Appendix</b>	<b>95</b>

# 1 Introduction

This work has been fully performed at *Aalto University*, at the department of *Chemical Engineering and Metallurgical Engineering* in the *School of Chemical Engineering*. Furthermore, the experimental results in (3.3.1 - Results ionic liquid separation) were provided to this thesis and not conducted by the author himself.

The thesis was submitted and presented at the *TU Wien*.

## 1.1 Background

In the textile industry cellulose fibers are used as materials to manufacture all different kind of clothing. As an effect of the growing world population, water is becoming scarcer and thus the affected industries need to reduce the cost of materials. In terms of cellulose-fibers for textile applications this means a decrease of the water consumption during the fiber production.

Nowadays, the viscose and lyocell process are the established techniques on a commercial scale. In the former, wood pulp is dissolved with sodium hydroxide (NaOH) and carbon disulfide (CS<sub>2</sub>), forming cellulose xanthates as intermediate products (Schaschke, 2014).

In the latter, cellulose is directly solved in N-methylmorpholine N-oxide (NNMO) without forming a previous derivative in a dissolution step (Mather and Wardman, 2015). Both technologies showed a significantly lower water consumption than cotton-made fibers fulfilling the requirements of future demand. However the use of toxic components (NNMO, Xanthates) pose a potential risk to the environment (Hämmerle, 2011).

In 2013, different ionic liquids were tested on cellulose dissolution (Parviainen et al.,

## 1 Introduction

2013). As a result, a new fiber production method has been developed using an ionic liquid (1,5-diazabicyclo[4.3.0]non-5-enium acetate, [DBNH][OAc]) as a solvent. This new fiber, named Ioncell-F, showed good results in the mechanical properties of the fiber. In a further study, several process steps were established (Sixta, 2015).

An agitated thin-film evaporator was implemented in the pilot-scale process to recycle ionic liquid under low-pressure conditions. The distillate stream consisted of 99% water, whereas the residue product contained the high viscous ionic liquid with a small water content (5 - 10%).

The process parameters were optimized empirically regarding separation efficiency. As a result, high jacket temperatures and low system pressures led to good separation results. In addition a single stage flash model was designed to predict the separation capacity of the evaporator (Ahmad et al., 2016).

## 1.2 Evaporators

The object of evaporation is the thermal separation of two phases. In most cases, the objective is to recover a solvent or concentrate a solution. Evaporators are classified in their type of heat transfer (conduction, convection and radiation) and contact with the heating medium (tubular heating surfaces, coils, jackets, direct contact, solar radiation). The two relevant types of evaporators for this work are the *falling film* evaporator and the *agitated thin film* evaporator. Thermal sensitive products are generally separated by those types of evaporators due to their short residence time (E.Minton, 1986).

### 1.2.1 Falling film evaporators

The feed enters at the top of the vertical evaporator, where it is evenly distributed into arranged small tubes, which outer walls are heated. The resulting temperature gradient between the wall temperature and the center of the tube initiates transport phenomena. The

more volatile component evaporates and the resulting vapor is separated from the liquid. The falling-film evaporator is suitable for applications where the temperature difference between heating medium and liquid is small ( $\Delta T_{max} = 14.4 \text{ K}$ ).

Due to gravity, the fast moving film flow results in a short residence time. Typical applications are the concentration of dairy productions, sugar solutions and black liquor (Glover, 2004).

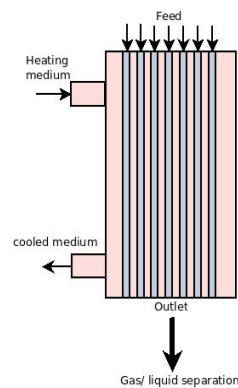


Figure 1.1: Falling film evaporation in single tubes with subsequent phase separation

### 1.2.2 Wiped film evaporators

Wiped film evaporators, also called agitated thin-film evaporators, are especially used for viscous materials. Normally, a wiped thin film evaporator operates with a short residence time and under low pressure to avoid to product degradation and high pressure drops. (Glover, 2004).

At the top of the vertical evaporator, the feed flows into a single tube, where rotating, axially arranged wiper blades lay out a thin film on the wall. The falling film is periodically remixed by those blades, which additionally enhances heat and mass transfer to the existing temperature gradient between the heated wall and the center of the tube (McKenna, 1995). The wiped film evaporator is limited in its applications due to high costs and requires a good heating medium since the heat surface area is relatively small. (SPX).

## 1 Introduction

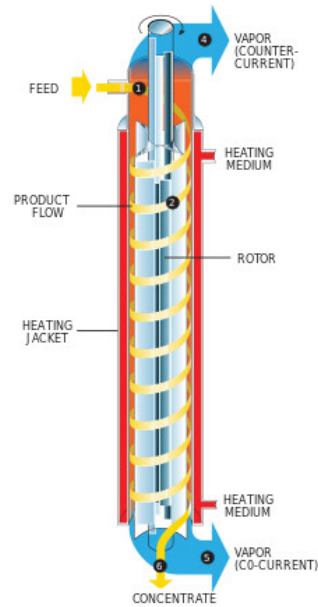


Figure 1.2: set-up of an agitated thin film evaporator(Icicorp)

## 1.3 Heat transfer

### 1.3.1 Falling film flow

A simple method to describe heat transfer in falling film flow is the use of empirical correlations of dimensionless numbers (Schmied, 2010).

$$Nu = C_1 Re^{C_2} Pr^{C_3}$$

with (1.3.1)

$$Nu = \frac{\alpha l^+}{\lambda} \quad Re = \frac{4\Gamma}{\mu} \quad Pr = \frac{c_p \mu}{\lambda} \quad l^+ = \left(\frac{\nu^2}{g}\right)^{\frac{1}{3}}$$

Equation (1.3.1) is generally referred as the *Nusselt correlation*. Depending on the flow regime, material parameters that are included in the dimensionless numbers (viscosity  $\mu$ , heat conductivity  $\lambda$ , density  $\rho$ ) and occurring evaporation (no boiling - boiling) determine the constants  $C_1$ ,  $C_2$  and  $C_3$ .

Table 1.1: Empirical coefficients for the Nusselt correlation for falling film Gourdon et al. (2015)

	$C_1$	$C_2$	$C_3$	Source
laminar	1.1	$-\frac{1}{3}$	0	Nusselt (1916)
laminar	1.3	$-\frac{1}{3}$	0	Schnabel and Schlünder (1980)
turbulent	0.0036	0.4	0.65	Numrich (1995)
turbulent	0.0030	0.4	0.44	Al-Najem et al. (1998)

The negative exponent of  $C_2$  in laminar falling film flow (with a linear temperature gradient in the film) takes into account the increasing resistance ( $\alpha_f = \frac{\lambda_f}{\delta_f}$ ) due to an increasing film thickness with an increasing Reynolds number.

In the case of turbulent flow, the temperature gradient in the film disappear for the most part. Only close to the wall there is a high temperature change that increases with higher flow velocities.

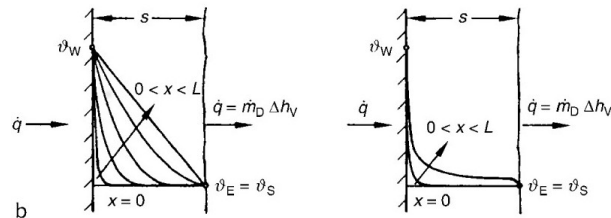


Figure 1.3: Temperature profiles in falling film evaporation for laminar (left) and turbulent (right) flow (Schnabel, 2010)

For the estimation of the heat performance of an evaporator in the absence of experimental data, different equations can be compared to each other yielding a certain range for the resulting heat transfer coefficient.

Numrich (1995) found a correlation that is valid for  $Pr < 52$ , whereas the other models in table 1.1 are limited to low Prandtl numbers ( $Pr < 10$ ). High Prandtl numbers indicate a poor thermal conductivity in the liquid phase being the main factor for heat transfer

## 1 Introduction

resistance in a falling film flow. Gourdon et al. (2015) showed that for high Prandtl numbers the assumption of laminar flow was incorrect.

Al-Najem et al. (1998) developed a numerical model based on differential equations for desalination. He assumed a steady state turbulent flow of an incompressible fluid with constant properties, a fully developed flow, negligible axial conduction and a uniform film thickness. The model predicted the local Nusselt number depending on the radius and height.

However, at the lower end of the evaporator the estimated heat transfer coefficient did not correlate with the experimental results. The model did not consider surface waves and interfacial shear stress, which were possible reasons for the deviation.

As mentioned, the constants of the Nusselt correlation are only valid for a certain flow regime. Five types depending on the Reynolds number section the whole flow range: *Purely laminar, first transition region, stable wavy flow, second transition region, fully turbulent flow* (Ishigai et al., 1974).

Chang (1994) describes possible wave regimes and the evolution of wave humps due to naturally and artificially excited evolution. As a reference, Dietze and Kneer (2010) extensive research on the flow separation in the capillary region of falling film treats waves dynamics in great detail. However, wave dynamics exceeds the outline of this thesis and the impact of waves is assumed to be negligible.

### 1.3.2 Energy balance

#### **Wassner model**

Evaporation being a thermal separation process, the energy balance is the point of interest regarding the heat performance. For the design of an evaporator the energy balance can be displayed as a function of the dimensionless numbers, thus giving a general formulation for an arbitrary geometry and material properties.



Wassner (1981) developed an elementary model for the design of falling film evaporators, defining the energy balance as a function of the temperature difference and the Nusselt number:

To simplify the system that had to be modeled, he assumed the following:

- steady state falling film flow
- uniform film thickness
- simple geometry - A hot medium (1) is condensing on the outer side of the wall (with a wall thickness  $s$ ) (2) heating the falling liquid (3) on the inside
- One-dimensional heat transfer
- no gradient along the flow
- Constant material properties, single phase

Thus, the heat flux  $\dot{q}$  is defined as function of the Temperature difference:

$$\dot{q}_i = \frac{\dot{Q}_i}{A_i} = \begin{cases} \alpha_i(T_i - T_{i+1}) = \alpha_i \Delta T_i & \text{if } i = 1, 3 \\ \frac{\lambda_i}{s}(T_i - T_{i+1}) = \frac{\lambda_i}{s} \Delta T_i & \text{if } i = 2 \end{cases} \quad (1.3.2)$$

The rate of heat flow  $\dot{Q}_i$  on both ends of the evaporator (film and condensing heating medium) depends only on the enthalpy of evaporation and the mass flow rate:

$$\dot{Q}_i = \dot{M}_i h_{i,vap} \quad | \quad i = 1, 3 \quad (1.3.3)$$

$$\frac{c_p(T_{i,in} - T_{i,out})}{h_{i,vap}} \ll 1$$

Assuming that the surface areas of all layers ( $A_i \sim A_{i+1}$ ) are approximately the same

## 1 Introduction

leads to a set of three equations:

$$\begin{aligned}\Delta T_2 - (1 + yNu_3)\Delta T_3 - \Delta T_1 &= 0 \\ -\Delta T_2 + (1 + x\frac{Nu_3}{Nu_1} + yNu_3)\Delta T_3 &= 0 \\ -x\frac{Nu_3}{Nu_1} + \Delta T_1 &= 0\end{aligned}\tag{1.3.4}$$

with  $x = \frac{\lambda_3}{\lambda_1} \left(\frac{\nu_1}{\nu_3}\right)^{\frac{1}{3}}$   $y = \frac{s}{\frac{\nu_1^2}{\nu_3^2}}$   $Nu_i = \frac{\alpha_i \left(\frac{\nu_i}{g}\right)^{\frac{1}{3}}}{\lambda_i}$

## Retrospective calculation

In the case of existing experimental data, the heat transfer can be derived from the mass balances of the falling film and the performance of the heater. For the latter, assuming that there is no phase change and constant temperature, for example an electrical heating jacket, the supplied energy can be defined as:

$$\dot{Q}_h = \alpha \Delta T\tag{1.3.5}$$

The required energy  $\dot{Q}_h$  is determined by the amount of evaporated liquid according to (1.3.3). The overall heat transfer coefficient can then be calculated for a known temperature difference  $\Delta T$  and its inverse is the sum of the inverse values of the single coefficients:

$$\frac{1}{\alpha} = \sum_{i=1}^k \frac{1}{\alpha_i}\tag{1.3.6}$$

### 1.3.3 Evaporation

Separation process units, as distillate columns or evaporators, are designed on the basis of thermodynamic equilibrium data. As a starting point, thermodynamic equilibrium is assumed.

The Gibbs phase rule defines for a given number of components (N) and occurring

Table 1.2: Different cases for ionic liquid evaporation with exemplary methods to determine the state of equilibrium

N	P	F	case	Correlation
1	2	1	water	Antoine equation
2	2	2	water + IL	Boiling point diagram
3	2	3	water+IL+hydrolysis product	

phases (P) the degree of freedom of the particular system.

$$F = N - P + 2 \quad (1.3.7)$$

However, it does not consider chemical reactions nor the impact of phase interfaces.

## Single component system

For a single vapor-liquid component system, the Antoine equation is used to describe the relation between the saturation vapor pressure and saturation temperature (Sinnott, 1999):

$$\ln(p_{sat}) = A - \frac{B}{T + C} \quad (1.3.8)$$

$A, B, C = const.$

## Multicomponent system

In a vapor liquid binary system (see table 1.2), the degree of freedom increases from 1 to 2. Additionally to a given temperature or pressure, a specific composition is needed to determine the state of equilibrium. Typically, VLE-diagrams are used to display the relation between the vapor and liquid phase (Pfennig et al., 2010)

## 1 Introduction

In general, the different models are categorized in equation of state models ( $\varphi - \phi$ ) and activity coefficient models ( $\varphi - \gamma$ ).

In the former the model defines a thermodynamic effective pressure  $f$  (fugacity) as a function of the fugacity coefficient  $\varphi$ . Examples are the ideal gas law or the Soave-Redlich-Kwong equation. Typically the  $\varphi - \varphi$  models are valid for a gaseous system.

$$f = \varphi \cdot p \quad (1.3.9)$$

The activity coefficient models are categorized in correlative models, where experimental discrete points are interpolated, as Wilson or NRTL, and predictive models, where no experimental data is needed, for example UNIFAC (Aalto, 2016). In analogy to the fugacity, the activity  $a_i$  (thermodynamical effective concentration) of one component is defined as the product of the activity coefficient  $\gamma_i$  and the specific mole fraction  $x_{m,i}$ .

$$a_i = x_{m,i} \gamma_i \quad (1.3.10)$$

In practice, process simulation software like Aspen Plus is used to calculate vapor liquid equilibria. For wiped film evaporation a model consisting of arranged flashes was designed in Aspen Plus (Lopez-Toledo, 2006).

## Boiling

Boiling usually takes place on the surfaces of tubes as a fluid flows through. If the liquid is boiling, the heat transfer is much higher than in the case of ordinary convection.

There are different types of boiling and different correlations are used to predict the heat transfer coefficient:

*Pool boiling* takes place at a solid surface submerged in a quiescent liquid. When the temperature of the solid surface,  $T_S$ , exceeds the saturation temperature of the liquid,  $T_{sat}$ , vapor bubbles form at nucleation sites on the surface and subsequently detach from the surface. The driving force for the heat transfer is the temperature difference,  $\Delta T_E = T_S - T_{sat}$ , called excess temperature.

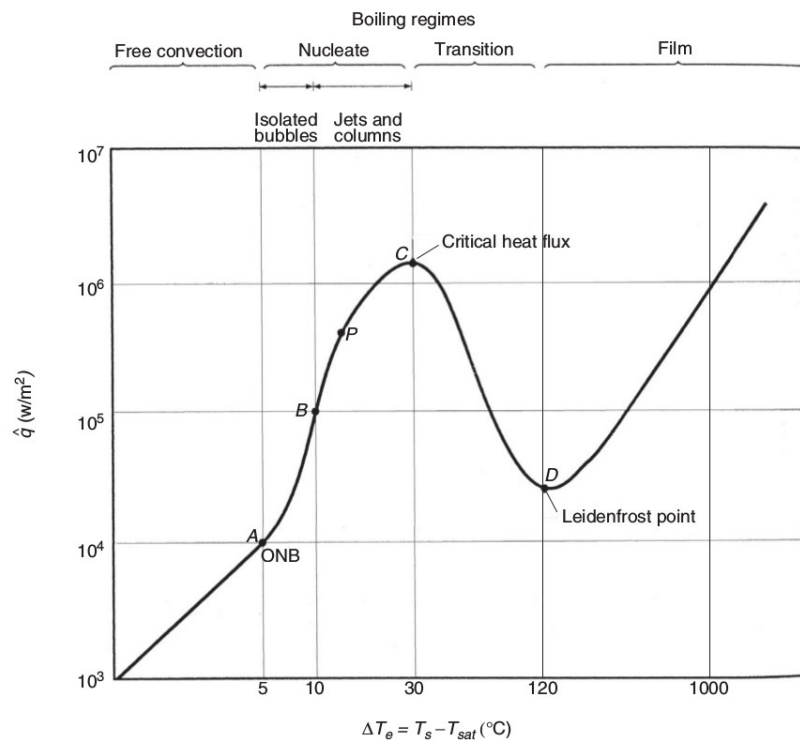


Figure 1.4: The boiling curve - the heat flux as a function of the excess temperature for different boiling regimes (Serth and Lestina, 2014)

The boiling curve summarizes the different boiling types for pool boiling. The heat flux normal to the solid surface,  $\dot{q}$ , is plotted as a function of the excess temperature.

In the nucleate boiling regime, the heat flux is proportional to the  $\Delta T_E$ . Vapor bubbles and jets induce turbulence and fluid mixing, leading to an increase in thermal conductivity. The maximum value of  $\dot{q}$  is determined by the critical heat flux,  $\dot{q}_c$ , marking the boundary line between *nucleate boiling* and *transition boiling*, where the heat flux starts to decrease with increasing wall temperature as a result of the smaller heat conductivity of the vapor.

In the transition zone the heat flux decreases with increasing  $\Delta T_E$  until it reaches a minimum value, called the *Leidenfrost point*, where a continuous vapor layer separates the solid surface from the liquid. Beyond this point *film boiling* occurs (Serth and Lestina, 2014).

Evaporation causes a two-phase flow consisting of a vapor and liquid component. For co-current flow in vertical tubes the different regimes can be categorized by the void fraction

## 1 Introduction

into *bubbly*, *slug*, *churn*, *annular* and *mist* flow (Serth and Lestina, 2014). The same types exist also for counter-current flows. However, the regime map is determined by the respective phase velocities (Kim et al., 2001)

## Vapor liquid interface

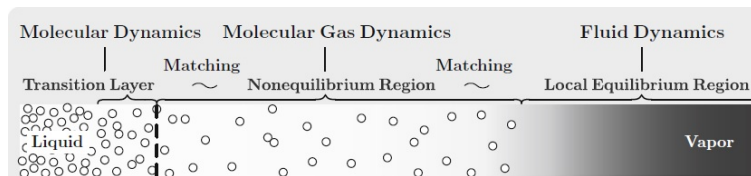


Figure 1.5: phase transition between the bulk liquid phase (left) and the bulk gas phase (right)

Fujikawa et al. (2011)

Evaporation, as a coupled phenomenon of mass and heat transfer, takes place at the interface between the liquid and vapor phase. However, on a microscopic level the interface consists of different layers. At its boundaries, there are bulk phases for both gas and liquid that are described by the thermodynamic equilibrium. In between there are two separate transition layers.

Whereas the bulk phases are described by the fundamental equations (e.g Navier-Stokes equation) that are also used in CFD modeling, the evaporation dynamics of the transition layer are derived from physical laws on a molecular level; The non-equilibrium region is described by the Boltzmann equation (Fujikawa et al., 2011).

### 1.3.4 Wiped film evaporators

In contrary to falling film flow, an analytical model for agitated thin film flow does not exist. Unterberg and Edwards (1967) suggested in their study about saline water evaporation a theoretical wiped film model with a linear temperature profile in the film. They assumed that evaporation would only take place at the free film surface. Heat transfer across the film

is caused by heat conduction and fully consumed by the latent heat of evaporation  $h_{vap}$ :

$$-\lambda \left( \frac{\partial T}{\partial r} \right)_{\delta_f} = h_{vap} \rho_l \frac{d\delta_f}{dt} \quad (1.3.11)$$

Furthermore, the impact of the wiper speed and feed flow rate was studied in a transparent evaporator. Below a certain wiper speed the liquid evaporated before the next blade arrived, leading to a vertical gaseous gap. Reducing the feed flow led to a smaller bow wave at a lower height of the evaporator.

McKelvey and Sharps (1979) gave an analytical approach to describe the flow in a bow wave of a wiped-thin film evaporator.

However, the coefficients of equation (1.3.1) are typically determined empirically. Bott and Romero (1963) defined a Nusselt Correlation by adding a second Reynolds number  $Re'$  that include the rotation speed ( $N$ ) of the blades:

$$Nu = 0.018 Re^{0.46} Re'^{0.6} Pr^{0.87} \left( \frac{d}{L} \right)^{0.48} n^{0.24} \quad (1.3.12)$$

$$Re' = \frac{d^2 N \rho_l}{\mu_l}$$

Abichandani and Sarma (1988a) established a relation between the Nusselt number and a blade factor ( $B_f$ ) that depended on the number of blades ( $B$ ), their single weight ( $m_B$ ) and the diameter of the evaporator ( $D$ ):

$$Nu_D = 0.0124 Re^{0.93} Re'^{0.35} Pr^{1.06} B_f^{-0.094} \quad (1.3.13)$$

$$B_f = \frac{B m_B g}{\mu N d^2}$$

The increase of the number of blades showed a similar effect as the increase of the rotational speed leading to a higher heat transfer coefficient of the film.

The comparison of the heavy and light blades showed no significant reduction of the heat resistance while the demand of electrical performance increased considerably. As a conclusion, light blades were preferred over heavy ones.

In a later paper Abichandani and Sarma (1988b) suspends the introduction of a blade factor. Instead, the number of blades was considered in the Nusselt correlation.

## 1 Introduction

For wiped film evaporator, an enhancement factor as the ratio between the film heat transfer coefficient of the wiped film ( $WF$ ) and the falling film evaporator ( $FF$ ) is used:

$$\beta = \beta(Re, Pr) = \frac{\alpha_{WF}}{\alpha_{FF}} \quad (1.3.14)$$

Lopez-Toledo proposes a model for a wiped film evaporator based on a series of stages of isothermal flashes. Its validity was limited to almost isothermal conditions ( $\Delta\theta < 1^\circ C$ ) and small concentrations of the volatile component in a binary mixture. The input variables were the evaporator geometry (diameter, length, wall thickness, thermal conductivity of the wall, number of blades), operational parameters (Feed rate, temperature, pressure, feed composition). An implemented UNIQUAC-program calculated the required activity coefficients for the flash stage (Lopez-Toledo, 2006).

## 1.4 Mass transfer

The available research on mass transfer of falling and wiped film evaporation is quite limited. As a short overview a few correlations and two evaporation theories are presented.

### 1.4.1 Falling film

Nielsen et al. (1998) provided a dimensionless correlation for mass transfer between a liquid and a gas phase in wetted wall columns (correction factor  $\zeta$ , inner diameter of the evaporator  $d_e$ )

$$Sh_l = 0.01613 \cdot Re_g^{0.01613} \cdot Re_l^{0.426} \cdot Sc_l^{0.5}$$

$$Sh_g = 0.00031 \cdot Re_g^{1.05} \cdot Re_l^{0.207} \cdot Sc_l^{0.5}$$

$$\text{for } 7500 < Re_g < 18300 \quad 400 < Re_l < 12000 \quad (1.4.1)$$

with

$$Sh_i = \frac{\beta_i \zeta d_e}{D_i} \quad Re_i = \frac{4\dot{V}_i \rho_i}{\pi d \mu_i} \quad Sc_i = \frac{\mu_i}{D_i \rho_i} \quad |i = g, l$$



Won and Mills (1982) defined a dimensionless liquid mass transfer coefficient including the Kapitza number:

$$\beta_l^+ = 6.97 \cdot 10^{-9} Re_l^{3.49} Cb^{0.27} Sc_l^{0.137} Cb^{-0.22} Cb^{-2}$$

with

$$\beta_l^+ = \frac{\beta_l}{(g \nu_l)^{\frac{1}{3}}} \quad Re_l = \frac{4\Gamma}{\mu_l} Sc = \frac{\nu_l}{D} \quad Cb = Ka^{\frac{1}{4}} = \nu_l \frac{\rho_l^3 g^{\frac{1}{4}}}{\sigma}$$
(1.4.2)

## 1.4.2 Wiped film

Lopez-Toledo (2006) defined one experimental correlation for the Sherwood number:

$$Sh_l = 1.53 \cdot Re_l^{0.51} \cdot Sc_l^{0.33} \cdot \left( \frac{d_e}{d_e - d_s} \right)^{0.44}$$

for  $1320 < Sc_l < 5810$   $2.94 < \frac{d_e}{d_e - d_s} < 7.2$

(1.4.3)

$d_e$  inner diameter of the evaporator  $d_s$  diameter of the blade

There are two established theories used to describe the mechanisms of mass transfer in agitated thin-film evaporation: The Billet theory and the Gropp & Schlünder theory:

### Billet's theory

A control volume similar to a rectification column is assumed. Falling liquid with a certain flow rate ( $\dot{L}$ ) is heated by a hot wall. At the interface to the rising vapor ( $\dot{V}$ ) evaporation occurs perpendicular to the flow. A mass balance of the more volatile component in a differentially small element  $dh$ , assuming equilibrium between the vapor and the liquid leads to the following equation:

$$\dot{L}^{sat} x_m = (\dot{L}^{sat} - d\dot{V}^{sat})(x_m + dx_m) + y^{sat} d\dot{V}$$

with  $d\dot{V} = d\dot{L}$

(1.4.4a)

$$\Rightarrow \dot{L}^{sat} x_m = (\dot{L}^{sat} - d\dot{L}^{sat})(x_m + dx_m) + y_m^{sat} d\dot{L}$$

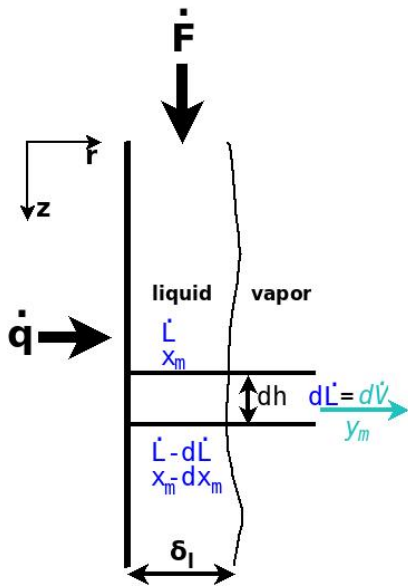


Figure 1.6: Billet's theory

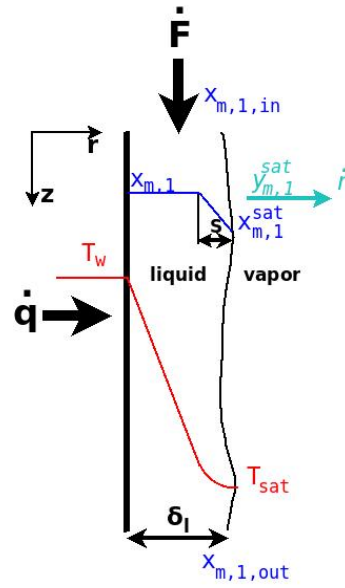


Figure 1.7: Gropp and Schlünder theory

separation of variables leads to:

$$\ln\left(\frac{\dot{L}_F^{sat}}{\dot{L}_R^{sat}}\right) = \int_{x_{m,R}}^{x_{m,F}} \frac{dx_m}{y_m^{sat} - x_m} \quad (1.4.4b)$$

Knowing the feed flow rate  $L_F$  and the molar fractions  $x_{m,F}$  and  $x_{m,R}$  one can calculate  $L_R^{sat}$  by solving the integral numerically. The average composition of the distillate can then be determined by applying the global mass balance:

$$x_{m,D} = \frac{L_F^{sat} \cdot x_{m,F} - L_R^{sat} \cdot x_{m,R}}{D} \quad (1.4.5)$$

## Gropp and Schlünder theory

The falling binary liquid is evaporated partially due to the heated wall surface. The more volatile component ( $x_{m,1}$ ) flows perpendicular to the falling film from the wall to the vapor-liquid interface where thermodynamic equilibrium is assumed.

Assuming one single thermodynamic equilibrium, the concentration gradient in  $z$  - direction is zero. The mass balance is solved for the concentration ratio,  $K_l$ , as a function

of the mass transfer coefficient  $\beta_l$  and the evaporation velocity of the liquid  $u_l$ . (Gropp and Schlünder, 1986).

$$K_l = \frac{y_{m,1}^{sat} - x_{m,i}}{y_{m,1}^{sat} - x_{m,i}^{sat}} = e^{-\frac{u_l}{\beta_l}}$$

$$\text{with } \beta_l = \frac{D}{S} \tag{1.4.6}$$

$$u_l = \frac{\dot{n}}{\rho_l} = \frac{\dot{n}}{\rho_l \Delta h_{vap}}$$

Regarding  $K$  as a function of  $\frac{u_l}{\beta_l}$ , two cases are of interest:

- $\frac{u_l}{\beta_l} \ll 1$ , in the case of very low velocities of evaporation the mole fraction at the interface is equal to mole fraction in the bulk
- $\frac{u_l}{\beta_l} \gg 1$ , in the case of very high velocities the concentration does not change along the film ( $y_1^{sat} = x_1$ ,  $K_l = 0$ ), The temperature at the interface is equal to the dew point temperature ( $T_{sat} = T_w(x_1, p)$ )

Dziak (2011) conducted experiments to verify the Billet theory by measuring the flow rates of the distillate and feed and the mole fraction of the distillate. In Billet's theory, a rectification effect was surmised, so the actual purity of the product would be higher than the theoretical estimation.

However, the experimental values were even lower than the theoretical values of the model, so the idea of a possible rectification effect was suspended.



## 2 Computational fluid dynamics

Taking falling film flow as an example, the Nusselt correlation is derived from physical assumptions. The coefficients and exponents of the Reynolds and Prandtl number are determined empirically, confirmed or improved by different scientific sources.

In computational fluid dynamics (CFD), fundamental equations of fluid mechanics constitute the basis for a specific model. They do not depend on a certain geometry or flow type making them a more universal tool to design engineering.

However, those governing equations are complemented by different other models, as turbulence models, which themselves depend on empirically determined coefficients. Furthermore, discretization schemes, bad choice of flow regime and boundary conditions can lead to arbitrary results.

### 2.1 Governing equations

Starting point for the governing equations are the conservation laws of fluid mechanics. A balance is made over a continuum in an elementary volume that is appropriately large compared to the molecular distances of the fluid.

There are two methods to formulate the equation: The Lagrangian approach, where the properties of a given elementary volume move in space and the Eulerian approach, where material properties are calculated as distributions over the spatially fixed control unit (Zikanov, 2011)

The governing equations are derived with the help of the Reynolds transport theorem

## 2 Computational fluid dynamics

which yields the general form of the balance equations (Mass, Momentum and Energy).

### 2.1.1 Reynolds transport theorem

Consider a physical quantity  $B$  defined in a time-dependent Volume  $V$ :

$$\frac{DB(t)}{Dt} = \frac{d}{dt} \int_{V(t)} b(t) dV \quad (2.1.1a)$$

thus, applying the Leibniz integral rule and  $b = \frac{B}{V}$ , yields the Reynolds theorem:

$$\frac{d}{dt} \int_{V(t)} b(t) dV = \int_{V_0} \frac{db}{dt} dV + \int_{A_0} b \mathbf{u} dA = \Omega \quad (2.1.1b)$$

if  $V$  approaches 0, the differential form is obtained:

$$\frac{\delta b}{\delta t} + \nabla \cdot (b \mathbf{u}) = \sigma \quad (2.1.1c)$$

$\sigma$  as a source term (Kuhlmann, 2007)

### 2.1.2 Conservation laws

The core of CFD models are the conservation laws of mass, momentum and energy. Their balance equations can be defined in a general way by rewriting equation (2.1.1c):

$$\frac{\delta}{\delta t} (\rho \hat{b}) + \nabla \cdot \underbrace{(\rho \mathbf{u} \hat{b})}_{C_{\hat{b}}} = \nabla \cdot \underbrace{(\Gamma \nabla \hat{b})}_{\delta_{\hat{b}}} + \sigma_{\hat{b}} \quad (2.1.2)$$

$C_{\hat{b}}$  is the convective flux of the field density  $\hat{b}$ .  $\delta_{\hat{b}}$  summarizes the diffusive flux as a result of the spatial distribution of  $\hat{b}$ . Typically,  $\delta_{\hat{b}}$  is modeled with a diffusion coefficient  $D$ .  $\sigma_{\hat{b}}$  includes all other sources or sinks. Table (2.1) summarizes the different terms of the governing equations.

The differential mass balance,

$$\frac{\delta \rho}{\delta t} + \nabla \cdot (\rho \mathbf{u}) = 0 \quad (2.1.3a)$$

also known as the continuity equation, reduces for incompressible flows to:

$$\nabla \cdot \mathbf{u} = 0 \quad (2.1.3b)$$

Table 2.1: general terms in the governing equations

	$b$	$\delta_{\hat{b}}$	$\sigma_{\hat{b}}$
Mass	1	0	0
Momentum	$\mathbf{u}$	$\nabla \cdot \boldsymbol{\tau}$	$-\nabla p + \rho g$
Energy	$h$	$-\nabla \cdot \dot{\mathbf{q}}$	$\frac{\delta \rho}{\delta t} + \nabla \cdot (\boldsymbol{\tau} \cdot \mathbf{u})$

Component mass balances can include a source term as long as the closing condition is fulfilled:

$$\begin{aligned} \frac{\delta \rho_k}{\delta t} + \nabla \cdot (\rho_k \mathbf{u}) &= \sigma_k \\ \sum_k \sigma_k &= 0 \end{aligned} \quad (2.1.4)$$

The Euler-equation is derived from the moment balance assuming no friction ( $\boldsymbol{\tau} = \mathbf{0}$ ):

$$\frac{\partial \rho_k}{\partial t} + \nabla \cdot (\rho \mathbf{u} \mathbf{u}) = \nabla p + \rho g \quad (2.1.5)$$

For incompressible flow a different form of the energy equation is used:

$$\rho c_p \left[ \frac{\partial T}{\partial t} + \nabla \cdot (\mathbf{u} T) \right] = -\nabla \cdot \dot{\mathbf{q}} + \boldsymbol{\tau} \nabla \mathbf{u} \quad (2.1.6)$$

## 2.2 Numerical computation

### 2.2.1 Discretization

In numerical engineering mathematical continuous functions, e.g. partial differential equations, in a certain domain, e.g. the geometry, are converted into a discrete form to enable computational solving. The discretization can be subdivided into three categories (Rusche, 2002),(Fletcher, 1997):

## 2 Computational fluid dynamics

- Equation discretization: Partial differential equations of the governing laws are transformed into algebraic terms. For example, in the finite difference method, the one dimensional heat equation

$$\frac{\partial T}{\partial t} = \frac{\lambda}{\rho c_p} \frac{\partial^2 T}{\partial x^2} = a \frac{\partial^2 T}{\partial x^2} \quad (2.2.1)$$

can be discretized as:

$$\frac{T_j^{n+1} - T_j^n}{\Delta t} = \frac{T_{j-1}^n - 2T_j^n + T_{j+1}^n}{\Delta x^2} \quad (2.2.2)$$

- Spatial discretization: The spatial domain is divided into a net of small cells. For each one the governmental equations are applied
- Time discretization: The time domain is split up into small time steps for transient problems.

### 2.2.2 Weighted residual methods

In the weighted residual methods, the solution of the considered partial differential equations are defined as a sum of analytical test functions  $\varphi_i$  and unknown coefficients  $a_i$ .

Thus the solution of the one dimensional heat equation yields: :

$$T(\mathbf{x}, t) = T_0(\mathbf{x}, t) + \sum_{i=1}^N a_i(t) \varphi_i(\mathbf{x}) \quad (2.2.3)$$

The coefficients have to be chosen in the suitable way, so that the error is minimized. The equation is written in its weak form,

$$L(T) = \frac{\partial T}{\partial t} - \frac{\lambda}{\rho c_p} \frac{\partial^2 T}{\partial^2} = \begin{cases} 0 & \text{for the analytical solution} \\ R & \text{for the approximate solution} \end{cases} \quad (2.2.4)$$

multiplied by a *weight function*  $W_m$  and integrated over the whole domain D:

$$\iiint_D W_m(\mathbf{x}) L dV = 0 \quad (2.2.5)$$



Table 2.2: Different weighted residual methods

Method	$W_m$	Description
Subdomain	$W_m = \begin{cases} = 1 & \text{for } x \in D \\ = 0 & \text{else} \end{cases}$	The computational domain is split up in m sub-domains
Collocation	$W_m(x) = \delta(x - x_m)$	the solution is solved for certain points, the collocation points $x_m$ , within the domain
Least-squares	$W_m = \frac{\partial R}{\partial a_m}$	argument of the integral is equivalent to $R^2$
Galerkin	$W_m = \varphi_M(\mathbf{x})$	$W_m$ contains the same type of functions as in R

Within the residual methods there are different approaches for the weight function (see table 2.2). The *finite volume method* is based on the sub-domain method, whereas the *finite elements method* is derived from the Galerkin method (Fletcher, 1997).

## 2.3 Finite volume method

A finite number of small control volumes form a grid covering the solution domain. Those control volumes consist of nodes situated in the center of the element containing physical properties. Cell faces connect adjacent elements.

### 2.3.1 Control volume

The solution domain is decomposed into a finite number of sub-domains, the control volumes. Together they form a grid generated by numerical algorithms. In principle, there are two approaches for the grid generation: The *cell* - and the *edge-oriented* structure. In the

## 2 Computational fluid dynamics

former the cell nodes are located in the cell center, in the latter the cell vertices are generated by connecting the nodes (Schäfer, 2006)

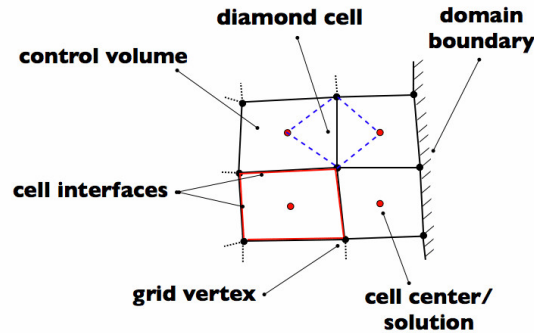


Figure 2.1: structure of a grid of finite volumes (Manzini, 2012)

The CFD model is solved for each control volume with a set of governing equations. Surface and volume integrals of the corresponding balance equations require face values as boundary conditions. Those values are interpolated from the cell core values with different interpolation schemes.

### 2.3.2 Interpolation

For a physical value  $\alpha$ , the node values are noted with capital letters, for example  $\alpha_D$ . Face values are marked by small letters (cardinal directions), for example  $\alpha_e$ .

The order of different interpolation schemes can be found out by comparing the order of the respective function with the equivalent Taylor series expansion:

$$\alpha_e(\mathbf{x}, e) = \sum_{n=0}^{\infty} \frac{\alpha^{(n)}(e)}{n!} (x - x_P)^n = \underbrace{\alpha_e}_{1^{st}} + \underbrace{\alpha'(e)(x - x_P)}_{2^{nd}} + \underbrace{\frac{\alpha''_e}{2}(x - e)^2}_{3^{rd}} + \dots \quad (2.3.1)$$

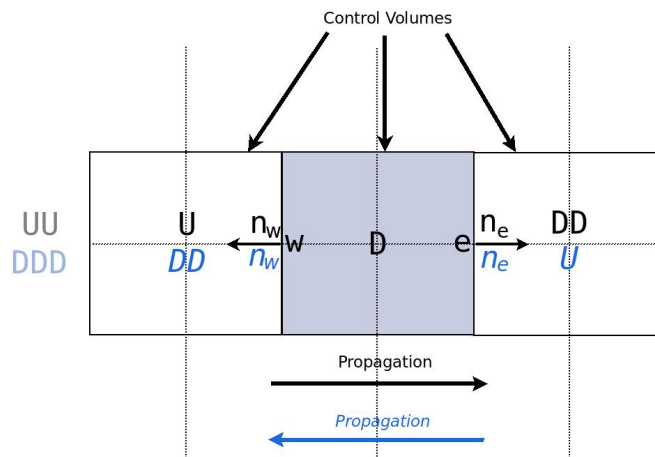


Figure 2.2: One dimensional grid in upwind notation, capital letters name node values, small letters interface values

## First order Upwind

Depending on the flow direction of the field quantity, a backward- or forward difference approximation is used:

$$\alpha_e = \begin{cases} \alpha_D & \text{if } (un)_e > 0 \\ \alpha_U & \text{if } (un)_e < 0 \end{cases} \quad (2.3.2)$$

The term *upwind* relates to the movement of a wave. Physical fluxes are represented by vector fields. Considering the flux as a one way flow the side of the flow origin is called Upwind.

The first order upwind scheme yields a truncation error often described as numerical diffusion. Particularly narrow gradients smear out unless the local grid quality is very high.

Higher upwind schemes exist that improve interpolation accuracy and reduce the truncation error by using a higher number of nodal points. They are usually referred as second-order or third-order upwind (Ferziger and Perić, 2002).

## Linear Interpolation

This scheme is a linear polynomial where an interpolation factor  $\lambda_e$  effectuates a linear distribution between two nodes:

$$\begin{aligned}\alpha_e &= \alpha_D \lambda_e + \phi_U (1 - \lambda_e) \\ \lambda_e &= \frac{x_e - x_U}{x_D - x_U}\end{aligned}\tag{2.3.3}$$

The linear interpolation is the simplest second order scheme and equals to the central-difference approximation of the first derivative (Ferziger and Perić, 2002).

## Quadratic Upwind - QUICK

The quadratic upwind scheme yields a parabolic interpolation and requires an additional nodal point:

$$\begin{aligned}\alpha_x &= \alpha_e = \alpha_U + g_1(\alpha_D - \alpha_U) + g_2(\alpha_U - \alpha_{UU}) \\ \text{where,} & \\ g_1 &= \frac{(x_e - x_U)(x_e - x_{UU})}{(x_D - x_U)(x_D - x_{UU})} \quad g_2 = \frac{(x_e - x_U)(x_D - x_e)}{(x_U - x_{UU})(x_D - x_{UU})}\end{aligned}\tag{2.3.4}$$

The quadratic interpolation scheme possesses a third-order truncation error. If it is used together with a second order integration, e.g. a surface integrals, the overall approximation is of second-order accuracy (Ferziger and Perić, 2002).

## Other schemes

Higher-Order interpolation schemes use higher-order polynomials for interpolation. They require more nodal values to determine the respective coefficients leading to higher number of equations to be solved and consequently to longer computation time. One should always consider critically the necessity of complex interpolation schemes.

On the one hand, high-order interpolation methods are accurate as long as the element is small enough. On the other hand, they tend to be less stable. A common systematic approach is to start with first-order schemes and gradually increase the order of the interpolation function.

Linear upwind schemes use two upstream nodes for linear extrapolation. As the central difference scheme, they are of second order. However, they are comparatively unstable due to unboundedness.

Scheme blending is used to increase the convergence in the case of oscillatory solutions. Typically, a lower - and a higher order scheme are combined and an additional solver parameter is implemented, for example, the Peclet number, to enable switching between the two schemes (Ferziger and Perić, 2002).

## 2.4 Finite element method

The finite element method has its roots in the field of structural mechanics. The two principal methods are the Ritz and the Galerkin method. For many fluid dynamic cases, the Galerkin method is applied.

Taking the one-dimensional heat equation (2.2.1) as an example, the approximate solution of the whole domain directly depends on the nodal values:

$$T = \sum_{i=1}^N T_i \varphi_i(x) \quad (2.4.1)$$

Whereas the finite volume method solves the governing equation for individual nodes in separate control volumes ( $W_m = 1$ ) for only one sub-domain, (see table 2.2), the finite element method provides a global system of equations. The functions  $\varphi_i$  are low-order polynomial functions that interpolate the local specific solution from the local nodal points (Fletcher, 1997).

The connection of those points form a mesh of finite elements. The procedure is

similar to the edge-oriented mesh generation in the finite volume method where the nodal points are situated on the vertices of the control volume.

## 2.4.1 General approach

### System of equations

A physical problem is described by a set of differential equations  $\mathbf{A}$ , a field function vector  $\boldsymbol{\alpha}$  within a closed Domain  $\Omega$  consisting of  $N$  sub-domains. At its edge,  $\Gamma$ , a set of boundary conditions  $\mathbf{B}$  is met:

$$\mathbf{A}(\boldsymbol{\alpha}) = \begin{bmatrix} A_1(\boldsymbol{\alpha}) \\ A_2(\boldsymbol{\alpha}) \\ \vdots \end{bmatrix} \quad \mathbf{B}(\boldsymbol{\alpha}) = \begin{bmatrix} B_1(\boldsymbol{\alpha}) \\ B_2(\boldsymbol{\alpha}) \\ \vdots \end{bmatrix} \quad (2.4.2)$$

$\boldsymbol{\alpha}$  is a column vector with  $j$  entries,  $j$  being the number of parameters, The one dimensional heat equation (2.2.1) yields for that syntax:

$$\boldsymbol{\alpha} = \alpha = T \quad (2.4.3a)$$

$$\mathbf{A}(T) = \left[ \frac{-\partial}{\partial x} \left( k \frac{\partial T}{\partial x} \right) + Q = 0 \right] \quad (2.4.3b)$$

$$\mathbf{B}(T) = \begin{bmatrix} T - T_\Gamma = 0 \\ k \frac{\partial T}{\partial n} - q_\Gamma = 0 \end{bmatrix} \quad (2.4.3c)$$

The finite element solution approximates  $\boldsymbol{\alpha}$  as a assembly of the nodal values and the interpolation functions:

$$\boldsymbol{\alpha} \sim \hat{\boldsymbol{\alpha}} = \sum_{i=1}^N \hat{\boldsymbol{\alpha}}_i \varphi_i \quad (2.4.4)$$

Most of the nodal values of  $\hat{\boldsymbol{\alpha}}_i$  are unknown, furthermore  $\varphi_i$  are independent variables. With the help of supplementary functions ( $\mathbf{G}_b$  and  $\mathbf{g}_b$ ), an integral equation is established to assemble the nodal values element by element:

$$\int_{\Omega} \mathbf{G}_b(\hat{\boldsymbol{\alpha}}_i) d\Omega + \int_{\Gamma} \mathbf{g}_b(\hat{\boldsymbol{\alpha}}_i) d\Gamma = \mathbf{0} \quad (2.4.5a)$$

Assuming that  $\mathbf{G}_b$  and  $\mathbf{g}_b$  are integrable follows:

$$\int_{\Omega} \mathbf{G}_b d\Omega + \int_{\Gamma} \mathbf{g}_b d\Gamma = \sum_{e=1}^N \left( \int_{\Omega_e} \mathbf{G}_b d\Omega + \int_{\Gamma_e} \mathbf{g}_b d\Gamma \right) = \mathbf{0} \quad (2.4.5b)$$

Equation (2.4.5b) is general expression that is solved both in the Galerkin and Ritz method. They differ in the way  $\mathbf{G}_b$  and  $\mathbf{g}_b$  are solved.

For a linear set of equation the finite element methods yields the following form:

$$\mathbf{K}\hat{\alpha} + \mathbf{f} = \mathbf{0} \quad (2.4.6)$$

Considering a linear elastic stress problem  $\mathbf{K}$  would be a stiffness matrix,  $\hat{\alpha}$  a displacement vector and  $\mathbf{f}$  an external force vector (Zienkiewicz, 2005).

## 2.4.2 Weighted residual methods - weak formulation

Mathematical differentiability classes rate function regarding their derivatives. A smooth function has an infinite number of continuous derivatives, denoted as in terms of differentiability. On the other side,  $C_0$  means a continuous function whose derivative is discontinuous.

For many physical problems the field function  $\alpha$  is not considered as a smooth function, for example a temperature gradient in a series of solid wall layers with different heat conductivity coefficients. In those cases, discontinuous derivation functions in the conservation laws occur which troubles numerical integration. However, with the use of test functions weak solutions of those differential equation can be expressed (Zienkiewicz, 2005).

A strong formulation:

$$\begin{aligned} \mathbf{A}(\alpha) &= 0 \\ \mathbf{B}(\alpha) &= 0 \end{aligned} \quad (2.4.7a)$$

is transformed into a weak formulation to

$$\int_{\Omega} \mathbf{v}^T \mathbf{A}(\alpha) d\Omega + \int_{\Gamma} \mathbf{v}^T \mathbf{B}(\alpha) d\Gamma = 0 \quad (2.4.7b)$$

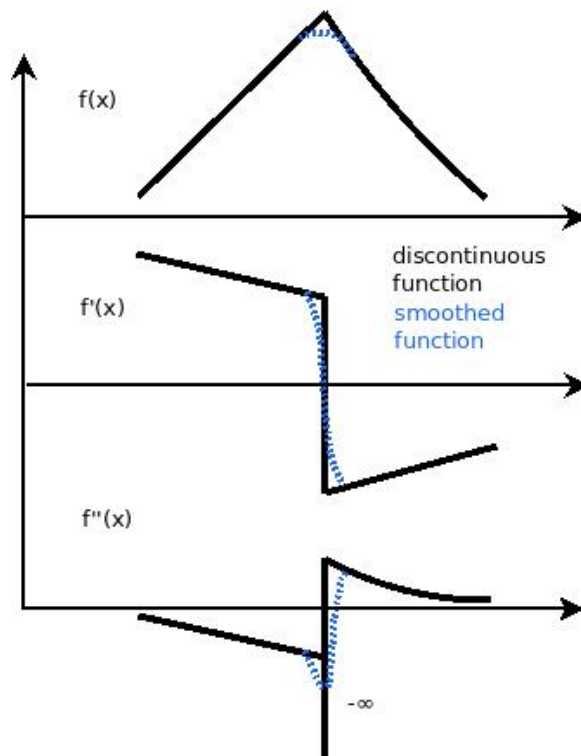


Figure 2.3: A  $C_0$  continuous function. The pole of the second derivative would cause an infinite integral impossible to solve numerically

with a so called test function  $\mathbf{v}$ :

$$\mathbf{v}^T = \begin{Bmatrix} v_1 \\ v_2 \\ \vdots \end{Bmatrix} \quad (2.4.7c)$$

Depending on the highest appearing derivative of  $n^{th}$ -order of  $\alpha$  in  $\mathbf{A}$  and  $\mathbf{B}$ ,  $\mathbf{v}$  has to be chosen in a way so that the  $n - 1$  derivatives are continuous. Another alternative form of the weak formulation exists:

$$\int_{\Omega} \mathbf{C}(\mathbf{v})\mathbf{D}(\alpha)d\Omega + \int_{\Gamma} \mathbf{E}(\mathbf{v})\mathbf{F}(\alpha)d\Gamma = 0 \quad (2.4.8)$$

Where the required differentiability of  $\alpha$  is lowered on behalf of higher differentiability of  $\mathbf{v}$  (Zienkewicz, 2005)



For example, the Poisson equation, in its strong form

$$\Delta\varphi = f \quad (2.4.9a)$$

is written in its weak form as:

$$\int_{\Omega} \Delta\varphi v d\Omega - \int_{\Omega} f v d\Omega = 0 \quad (2.4.9b)$$

with the Green's identity equation (2.4.9b) yields

$$\int_{\Omega} \Delta\varphi \Delta v d\Omega - \int_{\Omega} f c d\Omega = 0 \quad (2.4.9c)$$

Thus, the highest derivative appearing in  $\varphi$  is of first-order instead of second.

### 2.4.3 Elements

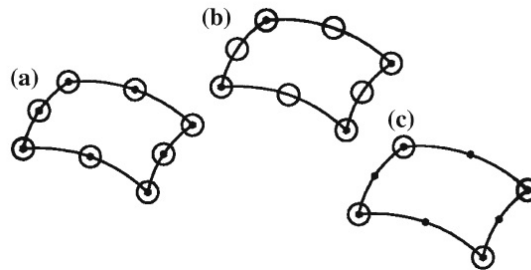


Figure 2.4: a) iso-parametric b) sub-parametric and c) super-parametric elements (Eslami, 2014)

There are a great number of different elements. However, only two parameters are needed to characterize an element type completely: the order of the approximating function and the order of geometric description. The former defines the degree of the shape function that interpolates the field values between the nodes. The latter the order of the polynomial characterizing the edges of the element.

For a one-dimensional element, the shape function and the geometric description are analogous to equation (2.4.4):

$$\hat{\alpha} = \sum_{e=1}^m \hat{\alpha}_e \hat{\varphi}_e s = \sum_{e=1}^n \hat{\alpha}_e^* X_e \quad (2.4.10)$$

Table 2.3: Examples of different one-dimensional elements in FEM

Method	Geometric description	Shape function	n-m
Straight linear	straight line (2 Nodes)	linear (2 Nodes)	0
Straight quadratic	straight line (2 Nodes)	quadratic (3 Nodes)	-1
Straight cubic	straight line (2 Nodes)	cubic (4 Nodes)	-2
Curved quadratic	Curve (3 Nodes)	quadratic (3 Nodes)	0
Curved cubic	Curve (3 Nodes)	cubic (4 Nodes)	-1

Depending on  $m$  and  $n$  an element can be categorized into iso – ( $n=m$ ), sub- ( $n<m$ ) and super-parametric ( $n>m$ ) elements.

In the same manner two dimensional - (triangular, quadrilaterals) and three dimensional (tetrahedrals, six-sided elements) are defined (Eslami, 2014)

## 2.5 CFD applications

The three most common CFD softwares used for fluid flow simulation with phase separation by evaporation are *Ansys Fluent*, *Openfoam* and *Comsol*. Since the latter two are considered in this thesis the following paragraph will give a short overview of their structure and related fields of application.

### 2.5.1 Introduction to Openfoam

OpenFOAM is an open source software based on C++. Its main focus is on fluid dynamic applications. However, other modules for different scientific areas exists. The program consists of a file system that is primarily divided into solvers, cases and utilities (Ltd).

Whereas the programing of OF solvers and utilities require an advanced knowledge of C++, the editing of cases is user-friendly and well-documented online. In the Openfoam

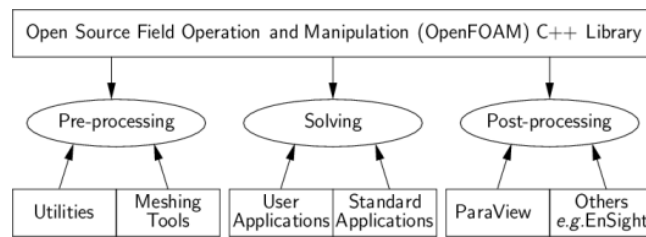


Figure 2.5: structure of Openfoam(CFDDirect, b)

cases the user can select an existing solver (isothermal, incompressible, reactions,..) depending on the physical problem to be modeled. Many tutorials on how to set-up a case in Openfoam are available online – as a reference the standard tutorials of CFD Direct explain quite well the structure of the OF cases (CFDDirect, a). After setting-up and solving those, the post processing (visualization, derivations,..) is typically done in Paraview, an open source application for scientific visualization (Paraview).

## 2.5.2 Introduction to Comsol

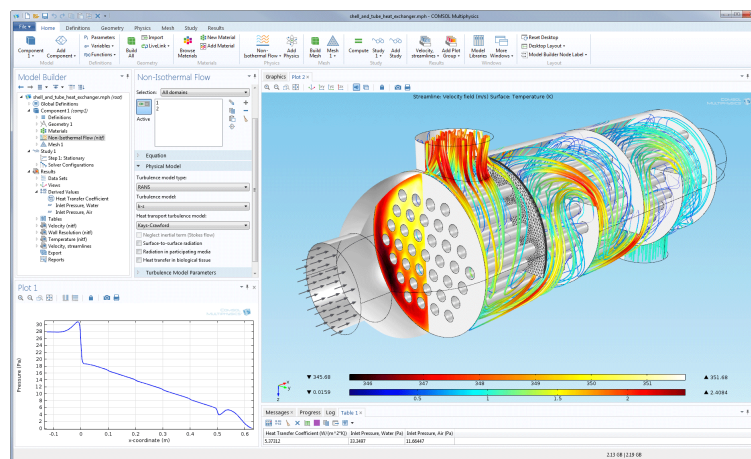


Figure 2.6: Graphical user interface in Comsol (Comsol, b)

Comsol Multiphysics is a commercial, modeling software with integrated graphical user interface. Unlike Openfoam, every step, e.g. pre-processing (geometry+ mesh), processing (e.g modeling system, set of equations, BC) and Post-processing (visualization of results)

## 2 Computational fluid dynamics

can be done without any additional software. There are specific modules for different applications, such as chemical, electrical, fluid flow or heat transfer. Integrated coupling functions allow the combining of different physical units if necessary. The model geometry can be imported from CAD-files or built with the implemented geometry module. In Comsol there are automatic and semi-automatic meshing tools – the default mesh type for 3D geometries is tetrahedral (Comsol, a)

### 2.5.3 CFD modeling in evaporation processes

In thin film evaporation two phases with two components occur. On the one hand the liquid has to be modeled with a proper multiphase model, on the other hand the evaporation dynamics require interface tracking of the liquid-gas boundary and integrated evaporation conditions and kinetics in the fluid flow.

Kharangate and Mudawar (2017) conducted an extensive literature search on phase change systems in CFD applications. Among other techniques, the survey discussed interface-capturing methods as the Volume of fluid method (VOF) and the Level-Set method (LSM).

Hardt and F.Wondra (2008) presented an evaporation model for interface-tracking methods to examine micro-scale evaporation phenomena. The model was evaluated with a VoF scheme on different evaporation cases like the Stefan problem.

Fontoura (2013) designed a CFD evaporation model in Openfoam for petrochemical pre-heaters to estimate the mass fraction of gas phase of crude oil due to cracking and evaporation in the pre-heater. They used a two-phase Eulerian multiphase model with a  $k-\epsilon$  turbulence model.

Zhou et al. (2013) used in their COMSOL model the level-set method to capture the behavior of bubbles during nucleate boiling of water in microchannels.

Ludwig and Dziak (2009) developed two models for isothermal laminar falling film flow in Comsol and Ansys Fluent. The level-set method was applied also and the film thickness

captured. However, the computation time of the Comsol model was longer and the deviation from the analytical result higher.

Pawar et al. (2012) studied the impact of the feed-rate on the concentration gradient in the bow wave of a concentrated sugar solution in an agitated thin film evaporator. A  $k - \epsilon$  and Reynolds stress model were used as turbulence models in Ansys Fluent. However, no evaporation source was included and instead constant volume fractions and material properties of the vapor and liquid were assumed.



# 3 Experiments

## 3.1 Set-up

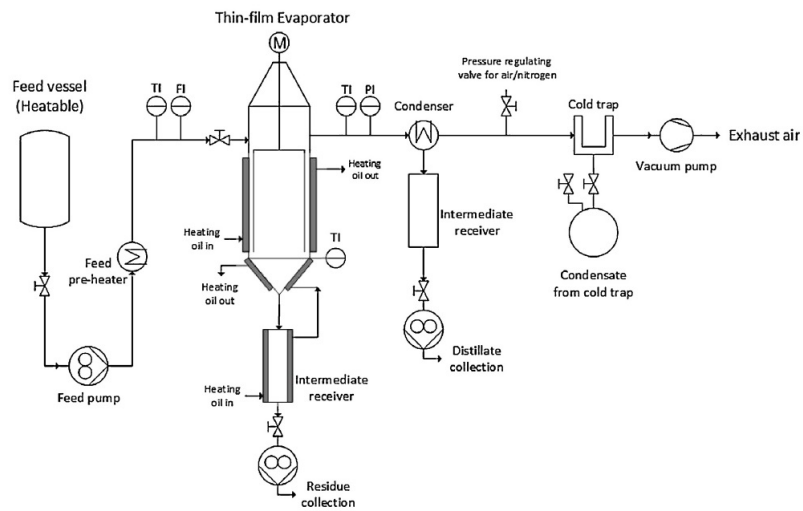


Figure 3.1: PI diagram of the process (Ahmad et al., 2016)

Figure 3.1 shows the PI-diagram of the thin-film evaporator that was used to obtain experimental results for validation. It is the same process unit that was used in (Ahmad et al., 2016).

The feed is stored in a glass tank from which a gear pump transports the liquid to the wiped film evaporator. A heat exchanger in between heats the liquid. Before entering the evaporation column the feed-rate,  $\dot{F}$ , and feed temperature,  $\theta_F$ , is measured. Other thermometers are found at the bottom and head of the column - the residue temperature,  $\theta_r$ , and distillate temperature  $\theta_d$ . The exiting vapor flows into a condenser which is kept almost at zero degrees Celsius to guarantee condensation at low pressure. To ensure that no water

### 3 Experiments

penetrates the vacuum pump an adjacent cold trap is installed in between. For further details the PID-drawing of the producer (UIC GmbH) is attached to the Appendix.

## 3.2 Water evaporation

In a previous master thesis (Burkhart, 2016), the operating conditions were optimized to obtain the highest separation factor  $\xi_{sep}$  possible in the separation of [DBNH][OAc] and water:

$$\xi_{sep} = \frac{\frac{x_{2,r}}{x_{1,r}}}{\frac{x_{2,F}}{x_{1,F}}} \quad (3.2.1)$$

No experimental design was used and the varying parameters were: The pre-heater temperature, the heating jacket temperature, the residue heater temperature, the temperature of the cooling medium, the pressure ( $p$ ) and the feed-rate.

As a starting point for this thesis a correlation analysis of those results was made. The residue ionic liquid concentration was inversely proportional to the feed-rate ( $r_{c_r, \dot{F}} = -0.95$ ) and partly proportional to heating jacket temperature ( $r_{c_r, \theta_h} = 0.83$ ) and residue temperature ( $r_{c_r, \theta_r} = 0.76$ ). However, the experimental information available was not sufficient to derive values for settings not previously used in the experiments.

For the modeling the knowledge of the heat transfer efficiency of the heater was crucial and a retrospective calculation (1.3.2) from the mass balance could not be made with the existing data provided. On the one hand, the results of the single cases varied too much, on the other hand the changes of the thermodynamic properties of the liquid mixture inside the evaporator were unknown.

For those reasons, further experiments were designed. First, the experiments were reduced to the single component evaporation of water to screen the parameters and determine a heat transfer coefficient for the evaporator. The pre and residue heater were switched off and the varying parameters were the feed-rate ( $\dot{F}$ ), Heating jacket temperature ( $\theta_h$ ) and pressure ( $p$ ). All other process parameters remained constant



### 3.2.1 Water evaporation results

Nine different ( all combinations of low and high values (8) and one setting with only averaged values were used. Each setting was repeated three times. Table 3.2 shows the values of the set parameters.

As output variables  $\theta_r$ ,  $\theta_d$  and the mass fractions  $\zeta_d$  and  $\zeta_r$  were noted down:

$$\zeta_D = \frac{m_d}{m_d + m_r} \quad (3.2.2)$$

Furthermore the equivalent saturation temperature  $\theta_{sat}$  for the operating pressure was calculated with the Antoine equation:

$$\theta_{sat} = \frac{1730.63}{8.07131 - \log(p \cdot [mmHg^{-1}])} - 233.426 \quad (3.2.3)$$

Table 3.1: experimental matrix of water thin film evaporation

Parameter	Low Value	High Value	Average value
$p$ [mbar]	20	60	40
$\theta_h$ [°C]	50	80	65
$\dot{F}$ [ $\frac{kg}{h}$ ]	5	7	6

### Fluctuation range

During an experiment the measured values were noted down every 10 minutes. After 30 minutes the evaporation was stopped. Only the initial values differed from the others and were not considered further. For the other time points ( $t = 10, 20, 30$  min) an overall averaged

### 3 Experiments

measure fluctuation was calculated:

$$\Delta x_{i,max-min} = \frac{\sum_j^9 \Delta x_{i,j,max-min}}{9}$$

$$\Delta x_{i,j,max-min} = \text{Max}(x_{i,j}) - \text{Min}(x_{i,j}) \quad (3.2.4)$$

with  $i$ ... parameter  $j$ ... noted value at time  $j$

Table 3.2: fluctuation range ( $\Delta x_{i,max-min}$ ) of measured parameters

$p$ [mbar]	$\dot{F}$ [ $\frac{kg}{h}$ ]	$\theta_h$ [ $^{\circ}C$ ]	$\theta_F$ [ $^{\circ}C$ ]	$\theta_r$ [ $^{\circ}C$ ]	$\theta_d$ [ $^{\circ}C$ ]
1	0.37	0.0	2.0	0.9	1.3

To determine the sample size ( $n$ ) a limit for a specific confidence interval of the distillate mass fraction  $\zeta_d$  was set:

The chosen significance level of  $\alpha = 0.05$  and the student's t-distribution were used. As a constraint, a maximum confidence band of  $\pm 3\%$  was defined:

$$CI = (\bar{\zeta}_d - t_{3,0.05} \frac{s}{\sqrt{n-1}}, \bar{\zeta}_d + t_{3,0.05} \frac{s}{\sqrt{n-1}}) \quad (3.2.5)$$

For  $n = 4$  all experiments fulfilled that requirement.

Table 3.3 shows the experimental results of the thin-film evaporation of water. There were slight variations in the feed-rate, but the operating pressure and heating jacket temperature had quite constant values. The residue temperature  $\theta_r$  has almost the same value as the respective saturation temperature  $\theta_{sat}$ . Additionally, the temperature difference between the heating jacket temperature  $\theta_h$  and saturation temperature  $\theta_{sat}$  was noted down ( $\Delta T^* = \theta_h - \theta_{sat}$ ).

Experiment 3 had the best evaporation results ( $\zeta_d = 85,73\%$ ) with a low feed-rate, low pressure, high heating jacket temperature and high  $\Delta T^*$ . The lowest distillate fraction was obtained in experiment 6 with a high feed-rate, high pressure and low heating jacket temperature

Table 3.3: averaged values of water evaporation with the confidence interval for  $\zeta_d$ 

Exp.	$p$ [mbar]	$\dot{F}$ [ $\frac{kg}{h}$ ]	$\theta_h$ [ $^{\circ}C$ ]	$\theta_F$ [ $^{\circ}C$ ]	$\theta_r$ [ $^{\circ}C$ ]	$\theta_d$ [ $^{\circ}C$ ]	$\theta_{sat}$ [ $^{\circ}C$ ]	$\zeta_d$ [ $\frac{kg}{kg}$ ]	CI	$\Delta T^*$ [ $^{\circ}C$ ]
1	20	5.05	50.0	24.5	17.1	20.5	17.5	37.7 %	1.4 %	32.5
2	60	4.96	50.0	24.3	36.0	36.3	36.2	13.1 %	1.2 %	13.8
3	20	4.92	80.0	24.4	17.0	20.0	17.5	85.7 %	2.8 %	62.5
4	20	7.13	50.0	23.9	16.5	20.7	17.5	28.5 %	1.8 %	32.5
5	60	4.93	80.0	24.0	35.9	36.2	36.1	63.4 %	1.3 %	43.9
6	20	6.83	80.0	24.3	17.2	20.3	17.6	62.7 %	0.8 %	62.4
7	60	7.12	50.0	23.2	35.9	36.2	36.2	8.5 %	1.3 %	13.8
8	60	6.91	80.0	24.0	36.0	36.3	36.2	45.7 %	2.7 %	43.8
9	40	5.93	65.0	24.0	28.8	29.2	29.0	39.6 %	1.6 %	36.0

### 3 Experiments

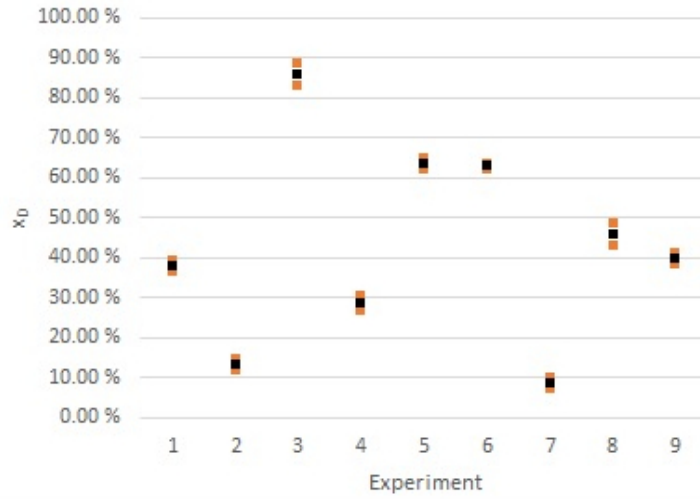


Figure 3.2: Water evaporation - averaged  $\zeta_d$  (blue) with confidence band (blue)

## Correlations

A correlation matrix from table 3.3 was generated and the correlation coefficients  $r_{i,j}$  calculated:

$$r = \frac{\sum_i^k (x_i - \bar{x})(y_i - \bar{y})}{s_x s_y} \quad (3.2.6)$$

The highlighted coefficients were categorized into very high ( $|r| = 1 - 0.91$ ), high ( $|r| = 0.90 - 0.71$ ) and moderate ( $|r| = 0.70-0.51$ ) correlations (see table 3.5). The operating pressure correlated fully with the measured temperatures ( $\theta_d, \theta_r, \theta_{sat}$ ), whereas the heating jacket temperature  $\theta_h$  had correlations with the distillate mass fraction  $\zeta_d$  and the temperature difference  $\Delta^*$ .

$r_{\dot{F}, \zeta_d} = -0.42$  indicates that the flow rate does not correlate with the distillate mass fraction. As a matter of fact higher feed rates, if  $\dot{F}$  is the only varying parameter, lead to lower distillate mass fraction (compare experiments 1 - 4 and 2 -7) Still the change is comparatively smaller compared to the influence of the operating pressure  $r_{p, \zeta_d}$ .

The correlation factors including the feed temperature  $r_{\theta_{\dot{F}}, j}$  indicate correlations without any physical meaning. It was kept constant around  $24^\circ C$  and had small random

deviations.

The ratio between temperature elevation  $c_p \Delta T^*$  and the enthalpy of evaporation  $h_{vap}$  for water show that the major part of the heating energy is used for the phase change (see table 3.4):

$$\text{with } \theta_{\dot{F}} = 24^\circ\text{C}, \quad c_p = 4185 \frac{\text{J}}{\text{kg K}} \quad h_{vap} = 2446 \cdot 10^3 \frac{\text{J}}{\text{kg}} \quad (3.2.7)$$

$$\text{for a given } \Delta T^* \Rightarrow \theta_{sat} = 24^\circ\text{C} + \Delta T^* \Rightarrow p$$

Table 3.4: heating-evaporation ratio  $\frac{c_p \Delta T^*}{h_{vap}}$  with corresponding saturation pressure (eq. (3.2.3))

$\Delta T^* [K]$	$\frac{c_p \Delta T^*}{h_{vap}} [\%]$	$p [mbar]$
1	0.17	31
10	3.42	90
50	8.55	370

The comparison of the correlation factors  $r_{p,\theta_r}$ ,  $r_{p,\theta_d}$ ,  $r_{\theta_h,\theta_r}$  and  $r_{\theta_h,\theta_d}$  show a strong relation between the pressure and the temperatures inside the evaporator, whereas the heating jacket does not have any influence on the residue and distillate temperature.

## Experimental overall heat transfer coefficients

For a rough estimation of the evaporator performance, an overall heat transfer coefficient  $\bar{\alpha}$  was derived from the mass balance, evaporator geometry (inner diameter  $d_e$  and height  $h_e$ ) and temperature difference between heating jacket temperature and saturation temperature:

$$\dot{Q}_{exp} = \dot{F}[c_p(\theta_{sat} - \theta_F) + \zeta_d h_{vap}]$$

$$\dot{q}_{exp} = \frac{\dot{Q}_{exp}}{A} = \frac{\dot{Q}_{exp}}{\pi d_e h_e} \quad (3.2.8)$$

$$\frac{\dot{q}_{exp}}{\theta_h - \theta_{sat}} = \bar{\alpha}_{exp}$$

### 3 Experiments

Table 3.5: Correlation matrix of the water thin film evaporation. Very Highly correlated coefficients are marked in solid green ( $0.90 < |r_{i,j}|$ ), moderate correlated coefficients have a transparent background ( $0.70 < |r_{i,j}| < 0.50$ )

.	$p$ [mbar]	$\dot{F}$ [ $\frac{kg}{h}$ ]	$\theta_h$ [ $^{\circ}C$ ]	$\theta_F$ [ $^{\circ}C$ ]	$\theta_r$ [ $^{\circ}C$ ]	$\theta_d$ [ $^{\circ}C$ ]	$\theta_{sat}$ [ $^{\circ}C$ ]	$\zeta_d$ [ $\frac{kg}{kg}$ ]	$\Delta T^*$ [ $^{\circ}C$ ]
$p$ [mbar]	1	0.00	0.00	-0.50	1.00	1.00	1.00	-0.42	-0.53
$\dot{F}$ [ $\frac{kg}{h}$ ]	0.00	1	-0.08	-0.63	-0.01	0.01	0.00	-0.33	-0.07
$\theta_h$ [ $^{\circ}C$ ]	0.00	-0.08	1	0.29	0.01	-0.01	0.00	0.85	0.85
$\theta_F$ [ $^{\circ}C$ ]	-0.50	-0.63	0.29	1	-0.5	-0.51	-0.51	0.55	0.52
$\theta_r$ [ $^{\circ}C$ ]	1.00	-0.01	0.01	-0.50	1	1.00	1.00	-0.42	-0.52
$\theta_d$ [ $^{\circ}C$ ]	1.00	0.01	-0.01	-0.51	1.00	1	1.00	-0.44	-0.54
$\theta_{sat}$ [ $^{\circ}C$ ]	1.00	0.00	0.00	-0.51	1.00	1.00	1	-0.43	-0.53
$\zeta_d$ [ $\frac{kg}{kg}$ ]	-0.42	-0.33	0.85	0.55	-0.42	-0.44	-0.43	1	0.95
$\Delta T^*$ [ $^{\circ}C$ ]	-0.53	-0.07	0.85	0.52	-0.52	-0.54	-0.53	0.95	1

In table 3.6 the temperature difference  $\Delta T_{sat,r}$  of the residue temperature  $\theta_r$  and saturation temperature  $\theta_{sat}$  was calculated. It varied from 0.2 to 0.9 K. As the deviation

Table 3.6: Comparison of the measured residue temperature with the corresponding saturation Temperature

Experiment	$\theta_r$ [ $^{\circ}C$ ]	$\theta_{sat}$ [ $^{\circ}C$ ]	$\Delta T_{sat,r}$ [K]	Experiment	$\theta_r$ [ $^{\circ}C$ ]	$\theta_{sat}$ [ $^{\circ}C$ ]	$\Delta T_{sat,r}$ [K]
1	17.1	17.5	0.4	6	17.2	17.6	0.4
2	36.0	36.2	0.2	7	35.9	36.2	0.3
3	17.0	17.5	0.5	8	36.0	36.2	0.2
4	16.5	17.5	0.9	9	28.8	29.0	0.2
5	35.9	36.1	0.2				

was small between those two parameters, the saturation temperature was assumed to be the occurring evaporation temperature in the thin film. Consequently the temperature difference between the entering feed temperature  $\theta_F$  and saturation temperature  $\theta_{sat}$  was taken as the relevant temperature elevation to derive the experimental heat transfer coefficient  $\bar{\alpha}$  (see equation 3.2.8).

Table 3.7: Experimental overall heat transfer coefficients during thin-film evaporation of water

Experiment	$\dot{F}$ [ $\frac{kg}{h}$ ]	$\theta_h$ [ $^{\circ}C$ ]	$\theta_{sat}$ [ $^{\circ}C$ ]	$\theta_F$ [ $^{\circ}C$ ]	$\zeta_d$ [ $\frac{kg}{kg}$ %]	$\dot{q}_{exp}$ [ $10^3 \cdot \frac{W}{m^2}$ ]	$\bar{\alpha}_{exp}$ [ $\frac{W}{m^2 K}$ ]
1	5.05	50	17.5	24.5	37.7	12.1	371.8
2	4.96	50	36.2	24.3	13.1	4.9	358.3
3	4.92	80	17.5	24.4	85.7	27.3	436.1
4	7.13	50	17.5	23.9	28.5	12.8	393.6
5	4.93	80	36.1	24.0	63.4	21.2	482.2
6	6.83	80	17.6	24.3	62.7	27.6	441.3
7	7.12	50	36.2	23.2	8.5	5.0	362.9
8	6.91	80	36.2	24.0	45.7	21.6	493.4
9	5.93	65	29.0	24.0	39.6	15.7	436.4

The overall heat transfer coefficient varies from 358.3 to 493.4  $\frac{W}{m^2 K}$ . There is a

### 3 Experiments

tendency of higher  $\alpha$  with higher heating jacket temperatures. One possible reason for this could be the temperature-dependent viscosity of the oil used in the heating jacket. According to the producer's website the heating medium Therminol 66 has a kinematic viscosity of  $2.96 \cdot 10^{-5} \frac{m^2}{s}$  at  $40^\circ C$ , which decreases to  $0.380 \cdot 10^{-5} \frac{m^2}{s}$  at  $100^\circ C$  (Therminol).

#### 3.2.2 Conclusions

For a better statistical evaluation of the correlation factors the range of variation has to be extended. From a physical point of view it is evident that there is a correlation between the feed-rate and distillate fraction, also the pressure seems to have only a little influence on the distillate mass fraction ( $r_{p,\zeta_d 0}$ ).

However, the before mentioned relations of pressure and heating jacket temperature prove that  $\theta_r$  and  $\theta_d$  do not depend on  $\theta_h$ .

In (Ahmad et al., 2016) the heating jacket temperature was taken as a the phase temperature for the single stage flash calculation in Aspen plus since the residue content of the VLE-data was close to the experimental results. However, the correlation analysis indicated a strong correlation of the pressure ( $p$ ) and the evaporator temperature ( $\theta_r, \theta_d$ ) instead. Therefore the assumption of  $\theta_h = \theta_r$  was suspended in the modeling.

## 3.3 Ionic liquid separation

The experimental results of the Ionic Liquid separation were used as validation cases for the designed model. With the known correlations of the water evaporation the number of different settings were reduced to a minimum as the evaporation of the binary required additional analytical analysis methods to determine the concentration of the feed, residue and distillate.



### 3.3.1 Results ionic liquid separation

A set of experiments with Ionic liquid – water separation was provided for this thesis. Every setting was repeated three times. The duration of each experiment was 30 minutes.

Table 3.8 shows the different settings of the experiments. As the feed is a binary liquid consisting of [DBNH][OAc] and water, the water content  $x_1$  (water being the more volatile component of the liquid), depending on the mass fractions within the feed, distillate or residue, was defined as a new parameter:

$$x_{1,i} = \frac{m_{1=H_2O,i}}{m_{1=H_2O,i} + m_{2=[DBNH][OAc],i}} \quad (3.3.1)$$

whereas,

$$\zeta_d = \frac{\dot{D}}{\dot{F}} \quad (3.3.2)$$

In table 3.9 the experimental values of the residue water content  $x_{1,r}$  were above the corresponding water content of the measured residue temperature  $x_1(\theta_r)$ . The water content was derived from the boiling curve of the provided vapor equilibrium data of the binary (see section 4.3.4).

Table 3.8: The four different experimental (E1-E4) settings of the IL separation

Parameter	E1	E2	E3	E4
$p$ [mbar]	15	15	15	15
$\theta_h$ [ $^{\circ}C_r$ ]	85	110	85	110
$\dot{F}$ [ $\frac{kg}{h}$ ]	3.6	3.6	3.6	3.6
$x_{1,F}$ [ $\frac{kg}{kg}$ ]	0.8	0.8	0.2	0.2

### 3 Experiments

Table 3.9: Experimental results of the IL separation

Parameter	E1	E2	E3	E4
$\zeta_d \left[ \frac{kg}{kg} \right]$	77.95 %	80.84 %	28.26 %	34.64 %
$CI_{\zeta_d} [1]$	3.78 %	2.16 %	13.02 %	5.43 %
$x_{1,r} \left[ \frac{kg}{kg} \right]$	14.08 %	11.77 %	8.82 %	8.57 %
$x_{1,d} \left[ \frac{kg}{kg} \right]$	98.1 %	96.8 %	93.5 %	84.1 %
$\theta_r [^{\circ}C]$	59.1	69.8	67.3	78.0
$x_{1,r}(\theta_r) \left[ \frac{kg}{kg} \right]$	8.0 %	6.3 %	6.7 %	5.2 %

### Fluctuation range

As in the water evaporation trials the measured values (t=10,20,30 min) were compared to each other and a measure fluctuation was determined according to equation (3.2.4):

Table 3.10: fluctuation range ( $\Delta x_{i,max-min}$ ) of measured parameters ionic liquid separation

$p [mbar]$	$\dot{F} \left[ \frac{kg}{h} \right]$	$\theta_F [^{\circ}C]$	$\theta_r [^{\circ}C]$	$\theta_d [^{\circ}C]$
1	0.14	5.4	8.6	6.3

### 3.3.2 Heat transfer coefficient

The overall experimental heat transfer coefficient was calculated by using a logarithmic temperature difference due to the varying saturation point of the ionic-liquid water binary:

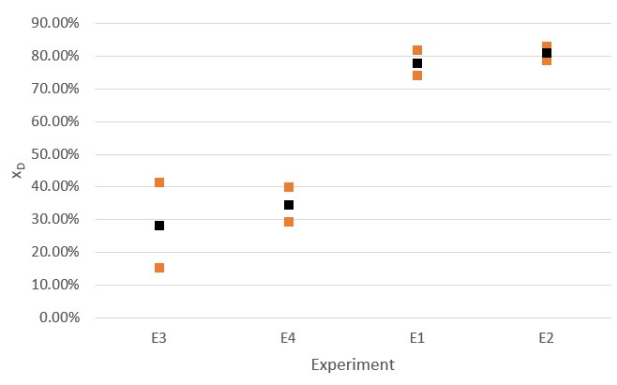


Figure 3.3: fluctuation range of the IL experiments

$$\bar{\alpha}_{exp} = \frac{\dot{q}_{exp}}{\Delta T_{ln}}$$

with

$$\dot{q}_{exp} = \frac{\dot{F} \zeta_d h_{vap}}{A_{evp}} \quad \Delta T_{ln} = \frac{(\theta_h - \theta_{F,sat}) - (\theta_h - \theta_{r,sat})}{\ln\left(\frac{\theta_h - \theta_{F,sat}}{\theta_h - \theta_{r,sat}}\right)}$$

(3.3.3)

Table 3.11: Experimental overall heat transfer coefficient  $\bar{\alpha}_{exp}$  of the Ionic liquid separation

Parameter	E1	E2	E3	E4
$\bar{\alpha}_{exp} \left[ \frac{W}{m^2 K} \right]$	438	311	189	150

The calculated overall heat transfer coefficients are, except from E1, significantly lower than those of the water thin-film evaporation.

### 3.3.3 Previous experiments

In (Ahmad et al., 2016) 10 different experiments with higher pressure (16-30 mbar), similar feed rates ( $2.1 - 4.3 \frac{kg}{h}$ ), ionic liquid concentration ( $x_2 = 20\%$ ) and heating jacket temperatures (around  $80^\circ C$ ) led to better results in terms of a lower water content ( $x_{1,r} = 5\%$ ). However, a pre-heater was used at  $80^\circ C$ .

### 3 Experiments

The comparison of E1 to similar experiments in (Ahmad et al., 2016) in table 3.12 show a difference between the residue mass fractions of the conducted experiments in this thesis and the published ones. In this thesis the models were compared to the conducted experiments .

Table 3.12: Comparison of E1 to experimental results in (Ahmad et al., 2016)

Parameter	E1	A6	A8	A9
$p$ [mbar]	15	31	21	16
$\theta_h$ [°C]	85	94	78	77
$\dot{F}$ [ $\frac{kg}{h}$ ]	3.6	4.08	3.59	4.30
$x_{1,F}$ [ $\frac{kg}{kg}$ ]	80 %	80 %	80 %	80 %
$x_{1,r}$ [ $\frac{kg}{kg}$ ]	14.08 %	5.31 %	5.01 %	5.01 %

#### 3.3.4 Conclusions

The higher value of the heating jacket set temperature had only a little effect on the liquid separation. A raise from 85 °C to 110 °C reduced the residue mass fraction from 14.08 % to 11.77 %.

However, the variation of distillate mass fraction within one setting indicates a certain variation. Also the residue temperature is not reaching a stationary value after 30 minutes. The extremely low heat transfer coefficient of  $150 \frac{W}{m^2 K}$  suggest strongly an error in the assumed temperature difference.

The water content in the residue was higher than in former experiments (see table 3.12). However, in the conducted experiments the pre-heater and residue heater were switched off, which is a possible reason for the deviation.

In table 3.9 the actual water content of the residue  $x_{1,r}$  was compared to the corresponding value of the boiling curve at the residue temperature  $x_{1,r}(\theta_r)$ . In every experiment

### 3.3 Ionic liquid separation

$x_{1,r}(\theta_r)$  was lower than  $x_{1,r}$ . Therefore the provided equilibrium data (see section 4.3.4) did not match with the final residue concentration.



## 4 Models

Three different models were developed ( $OpenFoam_{H_2O} = OF_{H_2O}$ ,  $COMSOL_{H_2O} = COM_{H_2O}$  and  $COMSOL_{IL/H_2O} = COM_{IL/H_2O}$ ). The water evaporation was modeled in two different models in Openfoam and COMSOL.

At the beginning, the wall temperature, as a boundary condition in the models, was assumed to be close to the heating jacket temperature as it was considered in (Ahmad et al., 2016). This led to an overrated heat transfer in the evaporator. The resulting interface temperature equaled a saturation point of some hundred millibars, whereas the experimentally measured operating pressure varied between 20 and 60 mbar.

An Openfoam solver was created based on the tutorial of Andersen (2011) to put the temperature profile of the liquid film into relation with the saturation pressure. The results showed a controversy between the model and experiments.

It was not possible to set up a working two-phase model with the level-set - or multiphase modules in Comsol.

On the one hand the evaporation mechanisms and respective constants were unknown, on the other hand the computational capacities were limited. The fact that the thin film (less than 1 mm thick) fills up only a volume of the evaporator (diameter 126 mm, height 262 mm) and the size of a sufficient refine grid (cell length smaller than the film length) made it impossible to generate a mesh for the whole evaporator geometry.

Instead, the thin-film evaporation was assumed to be a column composed of ideal stages. In the  $COM_{H_2O}$  model, the evaporation of sole water was modeled ( $x_1 = 1 = const$ ), hence the evaporator model consisted of only one ideal stage. In the  $COM_{IL,H_2O}$  model the boiling temperature of the falling film changed with the decreasing water content  $x_1$ . Therefore

## 4 Models

a series of ideal stages was designed for the ionic liquid purification.

Furthermore, it was not possible to implement all material properties as changing variables into  $COM_{H_2O}$  the model, so that a continuous evaporation over the whole evaporator length would have been realizable. Additionally, it would have required a module for the water content  $x_1$  as a process variable to describe the changing consistency of the binary liquid.

### 4.1 $OF_{H_2O}$ model

Although there is a level-set method implemented in Comsol, no interface tracking method with evaporation cases was found. All multiphase cases are modeled in dispersed models as the euler-euler or mixture model. However, for the thin-film evaporation the latter seems to be inapplicable due to the extreme thin film thickness.

Hardt and F.Wondra (2008) gave a summary over evaporation methods for the volume of fluid and level-set method. As already mentioned in section 2.5.3 similar processes to the thin-film evaporation were modeled in Openfoam and Fluent. Haider (2013) mentioned three different openfoam solvers used for evaporation cases: *interFoam*, *compressibleinterFoam* and *interphaseChangeFoam*.

The latter was chosen for this thesis as there was already a phase-change algorithm implement in the solver. In the InterphaseChangefoam solver the fluid properties are calculated as a mixture of the components. Only one momentum equation is solved. The flow model can be chosen by the user (laminar, RAS, LES) and the phase-change model is originally designed for cavitation cases (Openfoam, 2016).

The tutorial Andersen (2011) adds a temperature and saturation pressure field to the solver. The temperature field is complemented by a governing equation for energy conservation:

$$\frac{\partial T}{\partial t} + \nabla \cdot \Phi T - \nabla \cdot \frac{\lambda}{\rho c_p} \nabla T = 0 \quad (4.1.1)$$

The saturation pressure is calculated as a function of the temperature with the



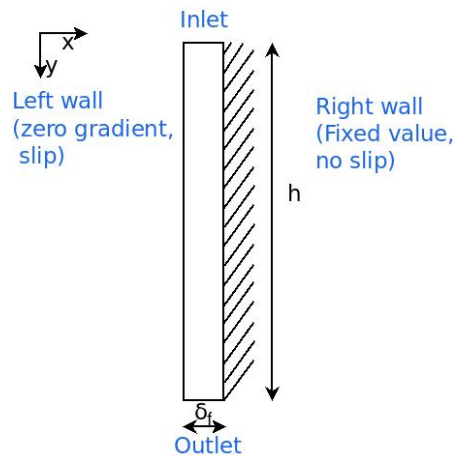


Figure 4.1: geometry of the thin-film case. A liquid film flowing down in between two walls

Roche-Magnus equation:

$$p_{sat} = 610.94 \cdot e^{\frac{17.625(T-273-15)}{T-30.11}} \quad (4.1.2)$$

The tutorial uses the Merkle mass transfer model to describe occurring condensation and vaporisation:

$$\begin{aligned} \dot{m}^- &= \frac{C_g \rho_g}{\frac{1}{2} u_\infty^2 t_\infty} \alpha \min(0, p - p_{sat}) \\ \dot{m}^+ &= \frac{C_l \rho_l}{\frac{1}{2} u_\infty^2 t_\infty} (1 - \alpha) \max(0, p - p_{sat}) \end{aligned} \quad (4.1.3)$$

where:

$C_g, C_l, u_\infty, t_\infty$  are empirical constants

The geometry of the Openfoam case was a two dimensional planar rectangle (0.17 • 100 mm<sup>2</sup>). On the right hand side of the rectangle the boundary conditions for a heated wall were set ( $T_h$ , no slip), on the other side a no-slip condition for the velocity and zero gradient conditions for p and T were defined.

For the fluid the properties of water were taken ( $\rho = 1000 \frac{kg}{m^3}$ ,  $\lambda = 0.591 \frac{W}{m K}$ ,  $\nu = 9 \cdot 10^{-7} \frac{m^2}{s}$ ). The default values of the solver for the mass transfer coefficient were not changed. All case settings with occurring evaporation (at lower pressure) did not converge to a solution.

#### 4 Models

Table 4.1: Boundary conditions of the OpenFoam case. The definitions of the boundary conditions can be found on (CFDDirect, 2017)

	$T$ [in $K$ ]	$p$ [in $bar$ ]	$U$ [in $\frac{m}{s}$ ]	$\alpha$ [in $\frac{m^3}{m^3}$ ]
Inlet	$T = 297.15$	zeroGradient	$v = 0.0446$	$\alpha = 1$
Outlet	zeroGradient	$p = 1$	pressureInletOutletvelocity	inletoutlet
Right wall	$T = 320.15$	zeroGradient	$\mathbf{u} = \mathbf{0}$	zeroGradient
Left wall	zeroGradient	zeroGradient	slip	zeroGradient

Therefore only the saturation pressure as a function of the temperature was evaluated without any phase change. As a result, the temperature gradient was practically zero (uniform film temperature) due to the low heat flux, thin film thickness and sufficient good heat conductivity of water. In other words, the temperature of the model iterated towards the fixed boundary value at the wall.

According to the Roche-Magnus equation, an assumed film temperature of  $85\text{ }^{\circ}\text{C}$  results in a vapor pressure of 751 mbar. Even at  $60\text{ }^{\circ}\text{C}$  the pressure at the saturation point would be 271 mbar which still is much higher than the operating pressure of 20 mbar which equals a boiling temperature of  $17.5\text{ }^{\circ}\text{C}$  for water. So assuming both, low pressure and the temperature of the heating jacket, in the film would lead in any case to a complete evaporation of the feed.

In every experiment of the water thin film evaporation (section 3.2.1) a certain amount of the feed flowed to the residue unevaporated. However, the model predicted a complete evaporation at the same conditions ( $\theta_h = 85\text{ }^{\circ}\text{C}$ ,  $p = 20\text{ mbar}$ ) as in the flash models in (Ahmad et al., 2016).

Those different results in the experiments and the model lead to a contradiction. As a consequence, the disposed assumptions were reviewed critically. The experimentally measured values showed that the corresponding saturation temperature of the pressure was close to the residue temperature (section 3.2.1), thus the measured pressure was assumed to be reliable.

The heating jacket temperature on the other hand was the indicated value of the respective thermostat. The steel wall between the evaporator basket and heating jacket and the heating oil itself were not considered as thermal resistances in the model.

From the experimental energy balance the order of the heat flux was estimated. In the model no phase change was considered, so the required heat flux in the model was much lower. Combining the two constraints of equilibrium conditions ( $\theta_f = \theta_{sat}(p)$ ) at the film surface and an experimentally determined heat flux through the falling film lead to the conclusion that there had to be a temperature gradient in the liquid.

As a model approach those two constraints (saturation temperature and heat flux at the film interface instead of a zero gradient) were implemented in the Comsol models.

## 4.2 $COM_{H_2O}$ model

In both, the  $COM_{H_2O}$  and  $COM_{IL,H_2O}$ , models the thin film evaporation was modeled as an ideal stage process. Whereas the  $COM_{IL,H_2O}$  model consisted of a multi-stage simulation due to the changing vapor pressure of the liquid film along the evaporator height, the evaporation of water was modeled as a single stage evaporation due to the constant boiling temperature of the water ( $p = const \Rightarrow \theta_{sat}(p) = const$ ).

The experimental results of the water evaporation were used to define a heat transfer coefficient,  $\alpha_h$ , of the heating jacket for the  $COM_{H_2O}$  model.

The *heat transfer* and *laminar fluid flow* module in COMSOL 5.2a were combined to model the thin film evaporation. Only the domain of the liquid film was considered. A grid independence study was performed to define a sufficient grid refinement with a short computational time. The velocity profile of the model was compared to an analytical solution.

The resulting heat transfer coefficient for the heating jacket was determined for the different experimental results. That heat transfer coefficient function then was used for the following ionic liquid model  $COM_{IL,H_2O}$ .

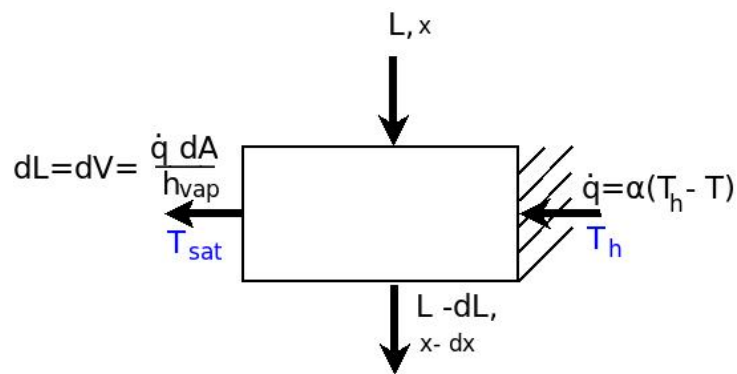


Figure 4.2: Principle of an ideal stage thin-film evaporation. A liquid falling film flow  $L$  evaporates due to a heat flux  $\dot{q}$ , the evaporated part  $dV$  leaves the domain of the liquid film. The blue values symbolize the fixed temperatures of the interface and heating jacket as boundary conditions

### 4.2.1 Analytical Solution

An incompressible liquid Newtonian fluid surrounded by a wall and a co-current gas is flowing down due to the gravitational force. The Navier Stokes equation yields for a two dimensional case ( $\mathbf{u} = (0, v, w)^t$ ), constant material parameters ( $\rho, \mu = const$ ) and stationary conditions:

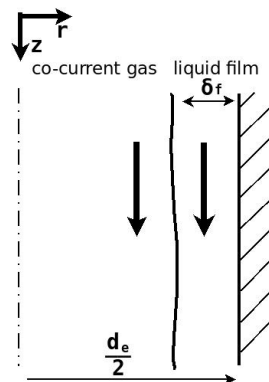


Figure 4.3: principle of falling film with co-current gas flow

$$\rho \mathbf{u} \cdot \nabla \mathbf{u} = -\nabla p + \mu \Delta \mathbf{u} + \rho g \quad (4.2.1)$$

A one dimensional flow ( $v = 0$ ) simplifies the continuity equation (2.1.3a) to:

$$\frac{\partial v}{\partial r} + \frac{\partial w}{\partial z} = 0 \quad \Rightarrow w = w(r) \quad (4.2.2)$$

Thus, for a negligible pressure gradient ( $\frac{\Delta p}{\Delta x} = 0$ ), equation (4.2.1) yields in z-direction:

$$\rho v \frac{\partial w}{\partial r} + \rho w \frac{\partial w}{\partial z} = \mu \left( \frac{\partial^2 w}{\partial r^2} + \frac{\partial^2 w}{\partial z^2} \right) + \rho g = 0 \quad (4.2.3)$$

which reduces to

$$\mu \frac{\partial^2 w}{\partial r^2} + \rho g = 0 \quad (4.2.4)$$

The no-slip condition at the wall and negligible shear stress at the interface provide two boundary conditions:

$$\begin{aligned} r = \frac{d_e}{2} \quad w &= 0 \\ r = \frac{d_e}{2} - \delta_f \quad \tau_{zr} &= \mu \frac{dw}{dr} = 0 \end{aligned} \quad (4.2.5)$$

The integration of (4.2.5) yields the velocity profile:

$$w(r) = w_{th}(r) = \frac{\rho g}{\mu} \left( \delta_f r + \frac{r^2}{2} \right) \quad (4.2.6)$$

## 4.2.2 Geometry

The model geometry consists of a uniform falling film area in a 2D axisymmetric space. The inner diameter  $d_e$  and height  $h_e$  of the evaporator are known from plant design,

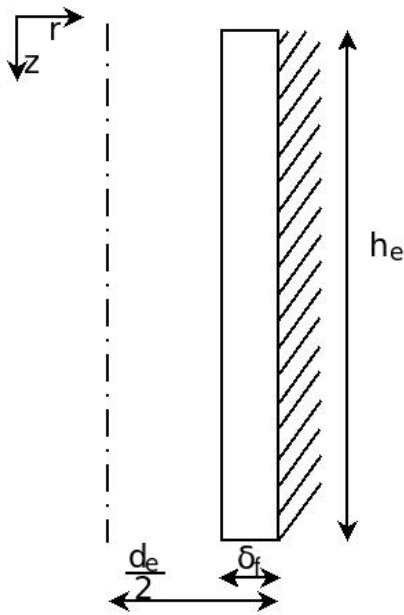


Figure 4.4: Evaporator geometry with thin-film area.

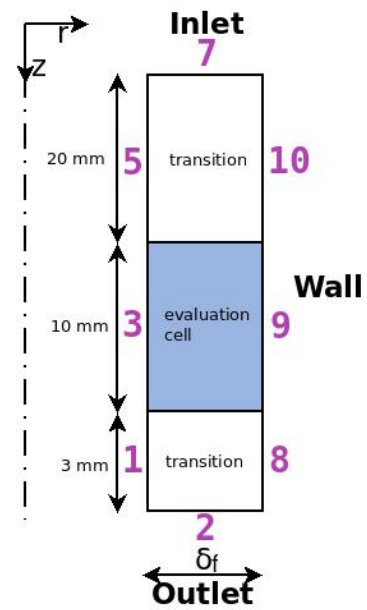


Figure 4.5: sections of the Comsol models. In purple the numbering of the element faces

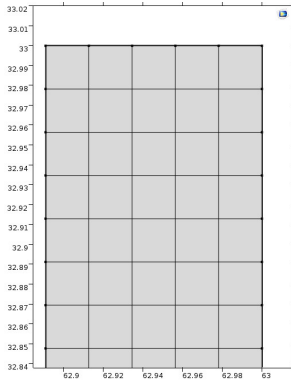
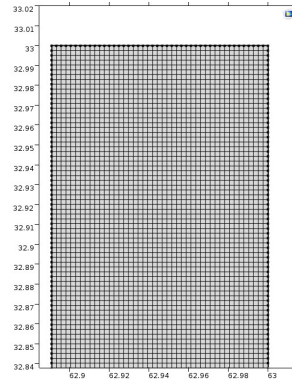
whereas the film thickness is calculated according to the Nusselt theory:

$$\delta_f = \left(\frac{\nu^2}{g}\right)^{\frac{1}{3}} Re^{\frac{1}{3}} \quad Re < 400$$

$$Re = \frac{\dot{F}}{\pi d_e \mu} \tag{4.2.7}$$

$$\delta_f = 0.109 \text{ mm} \quad Re = 4.21 \quad \text{for} \quad \dot{F} = 6 \frac{\text{kg}}{\text{h}}$$

The falling film area is divided into three sections, two transition sections on the top and bottom and one evaluation cell in between. This arrangement was chosen due to the boundary conditions of the heat transfer module that disables a developed flow at the inlet face of the model.

Figure 4.6: Refinement at  $n_{grid} = 5$ Figure 4.7: Refinement at  $n_{grid} = 45$ 

### 4.2.3 Grid independence study

For the grid independence study only the laminar flow module is used to determine the velocity profile. A mass flow inlet boundary condition (at inlet  $\dot{M} = \int \rho(\mathbf{u} \cdot \mathbf{n}) d_e d_{DC} dS$ ), a no-slip condition ( $\mathbf{u}_w = \mathbf{0}$ ) at the wall and a slip condition at the interface boundary were defined.

To determine the appropriate refinement of the meshing a grid independence study was performed. A Comsol model for laminar falling film flow without evaporation and constant material parameters was set up, solved and compared to the theoretical velocity profile (equation 4.2.6)

#### Grid

A mapped mesh was used for the model (uniform cell quality 1). Three different grid refinements were tested. As a parameter a characteristic refinement number  $n_{grid}$  was defined:

$$n_{grid} = \frac{\delta_f}{\text{cell length}} \quad (4.2.8)$$

A parametric sweep ( $n_{grid} = 5, 25, 45$ ) was specified in the solver. The error between

#### 4 Models

the velocity profiles (for  $w(r)$  at  $z = 10\text{mm}$ ) of the model and the analytical solution were compared to the analytical solution. For  $n_{grid} = 25$  and  $n_{grid} = 45$  the average deviation  $avg(\frac{w-w_{th}}{w})$  was below 0.1 %.

Table 4.2: Deviation of the model values from the analytical solution for different  $n_{grid}$

$n_{grid}$	total number of elements	computation time	avg $(\frac{w-w_{th}}{w})$	max $(\frac{w-w_{th}}{w})$
5	7590	4 s	0.375 %	0.364 %
25	189 600	1 min 4 s	0.092 %	1.142 %
45	614 205	12 min 16 s	0.071 %	0.164 %

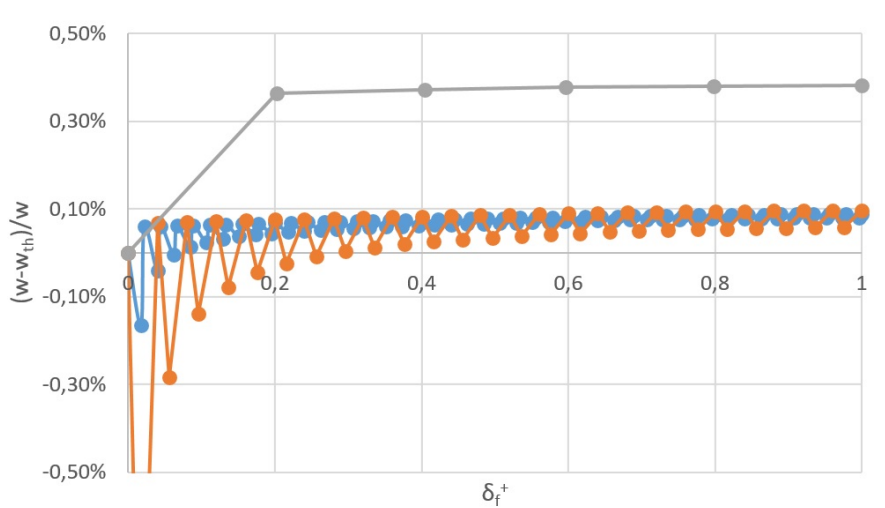


Figure 4.8: Deviation of  $w$  along  $\delta_f^+$

From the results of the grid independence study (table 4.2) a value of  $n_{grid} = 25$  was chosen due to short computation time and a small deviation margin after the first 4 values. Between  $n_{grid} = 25$  and  $n_{grid} = 45$  the average error decreased from 0.092 % to 0.071 %, whereas the computation time increased from 64 s to 736 s. Since the measured values of the feed rate had a fluctuation range of  $0.37 \frac{kg}{h}$  at a set value of  $3.60 \frac{kg}{h}$ , the relative value of the fluctuation ( $\frac{0.37}{3.6} = 10.3\%$ ) was much higher than the deviation of the model. However,  $n_{grid} = 25$  was chosen over  $n_{grid} = 5$  as the computation time was still relatively short. any



Figure 4.8 shows the error of the single elements along the dimensionless film length scale ( $\delta_f^+ = \frac{d_e - r}{\delta_f}$ ).

#### 4.2.4 Modules and boundary conditions

The heat transfer and laminar fluid flow modules were used for the water evaporation model. The setup (boundary conditions, material functions) of the  $COM_{H_2O}$  model is the same as in the  $COM_{IL,H_2O}$  model (see section 4.3.3).

The heating jacket was modeled with an integrated heat flux condition in Comsol. For that condition a heat transfer coefficient,  $\alpha_h$ , and an exterior temperature,  $\theta_{ext} = \theta_h$  were needed to define a heat flux over the heated wall boundary (lines 8,9 and 10 in figure 4.5).

$$\dot{q} = \alpha_h(\theta_{ext} - \theta) \quad (4.2.9)$$

On the film interface (lines 1,3, 5 in figure 4.5) the saturation temperature was set as a boundary condition. For the laminar flow an evaporation velocity,  $v$ , was defined at the liquid-gas interface:

$$v = \frac{\dot{q}_r}{h_{vap} \rho} \quad (4.2.10)$$

with  $\dot{q}_r$  heat flux in r-direction

From this velocity  $v$  the average value over line 3 was taken and a distillate mass fraction  $\zeta_d$  derived:

$$\bar{v} = \frac{\int v dz}{z} \quad (4.2.11)$$

$$\zeta_d = \frac{\dot{m}_{vap}}{\dot{F}} = \frac{\bar{v} \rho A_e}{\dot{F}}$$

#### 4.2.5 Determination of the heat transfer coefficient

For every experiment the heat transfer coefficient  $\bar{\alpha}_{mod} = \alpha_h$  of the heat flux boundary condition was determined to predict the experimental distillate mass fraction in the model

#### 4 Models

Table 4.3: Heat transfer coefficients during thin-film evaporation of water: modeled and experimental values

Exp	$p$ [mbar]	$\dot{F}$ [ $\frac{kg}{h}$ ]	$\theta_h$ [ $^{\circ}C$ ]	$\zeta_d$ [ $\frac{kg}{kg}$ %]	$\bar{\alpha}_{mod}$ [ $\frac{W}{m^2 K}$ ]	$\bar{\alpha}_{exp}$ [ $\frac{W}{m^2 K}$ ]
1	20	5.05	50	37.7 %	417	472
2	60	4.96	50	13.1 %	320	358
3	20	4.92	80	85.7 %	490	436
4	20	7.13	50	28.5 %	450	394
5	60	4.93	80	63.4 %	496	482
6	20	6.83	80	62.7 %	496	441
7	60	7.12	50	8.5 %	297	363
8	60	6.91	80	45.7 %	506	493
9	40	5.93	65	39.6 %	459	436

$$(\zeta_{d,mod} = \zeta_{d,exp}).$$

Both heat transfer coefficients, the experimental  $\bar{\alpha}_{exp}$  and modeled  $\bar{\alpha}_{mod}$ , showed a certain correlation with the heating jacket temperature ( $r_{\theta_h, \bar{\alpha}_{mod}} = 0.81$ ,  $r_{\theta_h, \bar{\alpha}_{exp}} = 0.91$ ). For that reason a linear temperature dependent function of the heat transfer coefficient was used for the ionic liquid – water separation model. The average values of  $\bar{\alpha}$  at the specific temperatures were taken as set points for the function:

$$\begin{aligned} \bar{\alpha}_{mod, \theta_h=50} &= 371 \frac{W}{m^2 K} \\ \bar{\alpha}_{mod, \theta_h=80} &= 497 \frac{W}{m^2 K} \\ \bar{\alpha}_{mod, \theta_h} &= \left( 371 + 4.2 \frac{\theta_h - 60^{\circ}C}{^{\circ}C} \right) \frac{W}{m^2 K} \end{aligned} \quad (4.2.12)$$

Also the correlation coefficient ( $r_{\bar{\alpha}_{exp}, \bar{\alpha}_{mod}} = 0.86$ ) showed that the model prediction is some way off the experimental results. Especially at low evaporation rates the deviation is high.

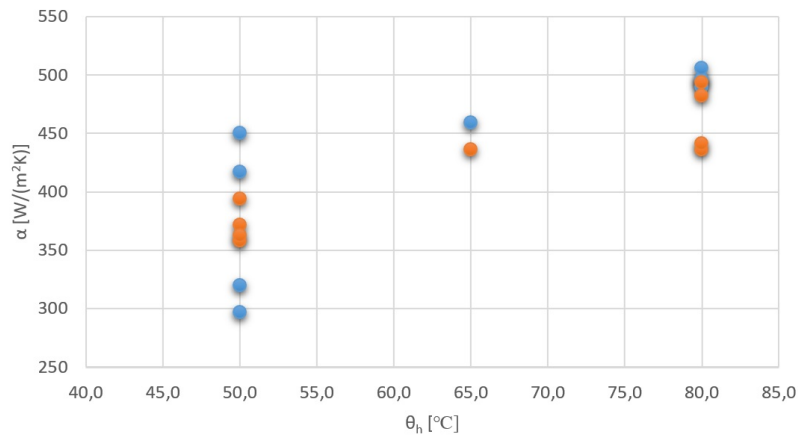


Figure 4.9: Heat transfer coefficients (blue-model, orange - experimental) at different temperatures

### 4.3 $COM_{IL/H_2O}$ model

A series of ideal stages was assumed and for each single stage the model was solved yielding discrete points of different process parameters as functions of the z-coordinate.

The thermodynamic properties of the [DBNH][OAc]-water binary were provided from the work of Ahmad et al. (2016). In particular, the boiling curves  $(T, x, y)$  for  $p = 15$  mbar and  $p = 20$  mbar were used. As the key parameter of the evaporation the saturation point temperature ( $\theta_{sat}$ ) as a function of the mass fraction  $x_1$  was chosen.

An interval of  $\Delta x_1 = 5\%$  between the single stages was set as the temperature elevation was small ( $\Delta T_{max} = 5$  K). For lower water contents ( $x_1 < 10\%$ ) the mass fraction step was  $2\%$ .

The input parameters were  $\theta_{sat}$ , the feed rate  $\dot{F}$ , water content  $x_1$  and heating jacket temperature  $\theta_h$ . The output parameters were categorized into constant parameters as material properties  $(\mu, \lambda, \rho)$  depending on the set mass fraction and temperature and variables (mass fraction, temperature, heat flux, velocity field) that were solved by the simulation.

The modeled stages yielded discrete points as a function of the water content ( $x_1$ ) that were interpolated linearly. Then by writing a mass balance the mass fraction was defined

## 4 Models

as a function of the z-coordinate. Four cases were compared to each other, the experimental results just providing the initial water content of the feed,  $x_{1,F}$ , and the residue content,  $x_{1,r}$ , at the bottom of the evaporator.

### 4.3.1 Geometry

The same geometry as in figure (4.5) with its corresponding sections was taken. A grid refinement of  $n_{grid} = 25$  was set.

### 4.3.2 Modules and boundary conditions

The default single phase laminar flow and heat transfer in fluids model were used. Table 4.4 summarizes the boundary conditions for the model:

Table 4.4: boundary conditions of the IL/H2O model

Line	Laminar flow	Heat transfer
2	Pressure outlet	film outflow ( $-\mathbf{n} \cdot \dot{\mathbf{q}} = 0$ )
7	Feed inlet ( $\int_{\Omega} \rho(\mathbf{u} \cdot \mathbf{n})d\Omega = \dot{m}$ )	Film inflow ( $T = T_F = T_{sat}$ )
1,3,5	Evaporation ( $v = \frac{\dot{q}_r}{h_{vap}\rho}$ )	Saturation point ( $T = T_{sat}$ )
8,9,10	Wall ( $\mathbf{u}_w = \mathbf{0}$ )	Heating jacket ( $\dot{q} = \alpha \Delta T$ )

The governing equations in the model were the momentum balance and heat equation :

$$\begin{aligned} \rho(\mathbf{u} \cdot \nabla)\mathbf{u} &= \nabla \cdot [-p\mathbf{I} + \mu(\nabla\mathbf{u} + (\nabla\mathbf{u})^T)] + \mathbf{F} + \rho\mathbf{g} \\ \rho\nabla \cdot \mathbf{u} &= 0 \end{aligned} \tag{4.3.1}$$

and

$$\rho c_p \mathbf{u} \cdot \nabla T + \nabla \cdot \dot{q} = \underbrace{\dot{Q}}_{\text{heat sources}} + \underbrace{\dot{Q}_p}_{\text{work by pressure changes}} + \underbrace{\dot{Q}_{vd}}_{\text{viscous dissipation}} \quad (4.3.2)$$

$$\dot{q} = -k \nabla T$$

### 4.3.3 Parameters

#### Process parameters

The process parameters were calculated for each stage and kept constant in the simulation. Each stage was defined by a water content  $x_1$  ( $x_1 = x_{1,F}$  at the top and  $x_1 = x_{1,r}$  at the bottom). The feed rate was calculated from the mass balance (see equation 4.3.3) and the film thickness of an ideal stage was expressed as a function of the feed-rate.

Table 4.5: Process parameters of the H20/IL model

Parameter	Value
Inner diameter of evaporator $d_e$	126 mm
Evaporator height $h_e$	262 mm
Feed-rate $\dot{F}$	const $\frac{kg}{h}$
Heating jacket temperature $\theta_h$	const $^{\circ}C$
Mass fraction water $x_1$	const $\frac{kg}{kg}$
Reynolds number $Re$	$Re = \frac{\dot{F}}{\pi d_e \mu} = 4.21$ for $\dot{F} = 6 \frac{kg}{h}$
Film thickness $\delta_f$	$(\frac{3\nu^2}{g})^{\frac{1}{3}} Re^{1/3}$ for $Re < 400$
Heat transfer coefficient of heating jacket $\alpha_h$	$163.78 + 4.2 \theta_h \frac{W}{m^2 K}$

## Material parameters

The material properties of pure [DBNH][OAc] were provided for this thesis. Only the heat conductivity was unknown. From (Albert and Mueller, 2014)  $\lambda_{[DBNH][OAc]}$  was estimated with  $0.1 \frac{W}{m K}$ .

The properties of water were taken from (DIPPR, 2015) as functions of the temperature.

Table 4.6: Material parameters of the H2O/IL model

Parameter	Value
Density $\rho$	$x_1 \rho_{H_2O} + (1 - x_1) \rho_{IL} [\frac{kg}{m^3}]$
Dynamic viscosity $\mu$	$x_1 \mu_{H_2O} + (1 - x_1) \mu_{IL} [Pa s]$
Specific heat capacity $c_p$	$x_1 c_{p,H_2O} + (1 - x_1) c_{p,IL} [\frac{J}{kg K}]$
Heat conductivity $\lambda$	$\frac{\lambda_{H_2O} \lambda_{IL}}{x_1 \lambda_{H_2O} + (1-x_1) \lambda_{IL}} [\frac{W}{m K}]$
Density of water $\rho_{H_2O}$	$1000 [\frac{kg}{m^3}]$
Density of ionic liquid $\rho_{IL}$	$1274.678 - 8.0964 \cdot 10^{-4} K^{-1} T_{sat} [\frac{kg}{m^3}]$
Dynamic viscosity of water $\mu_{H_2O}$	$e^{-52.843 + \frac{3793.6 K^{-1}}{T_{sat}} + 5.866 \log(\frac{T_{sat}}{K})} [Pa s]$
Dynamic viscosity of ionic liquid $\mu_{IL}$	$1.7 \cdot 10^{-8} K^{-4} T_{sat}^4 [K^{-4}] - 2.4 \cdot 10^{-5} K^{-3} T_{sat}^3 + 1.2 \cdot 10^{-2} K^{-2} T_{sat}^2 - 2.9 K^{-1} T_{sat} [Pa s]$
Specific heat capacity of water $c_{p,H_2O}$	$276370 - 2090 K^{-1} T_{sat} + 8.125 K^{-2} T_{sat}^2 - 0.0141 K^{-3} T_{sat}^3 + 9.37 \cdot 10^{-6} K^{-4} T_{sat}^4 [\frac{J}{kg K}]$
Specific heat capacity of ionic liquid $c_{p,IL}$	$1.826 - 5.561 e^{-3} K^{-1} T_{sat} [\frac{J}{kg K}]$
Heat conductivity of water $\lambda_{H_2O}$	$(-0.432 + 0.0057255 K^{-1} T_{sat} - 8.078 \cdot 10^{-6} K^{-2} T_{sat}^2 + 1.861 \cdot 10^{-9} K^{-3} T_{sat}^3) [\frac{W}{m K}]$
Heat conductivity of ionic liquid $\lambda_{IL}$	$0.1 [\frac{W}{m K}]$
heat transfer coefficient of heating jacket $\alpha_h$	$163.78 + 4.2 \theta_h [\frac{W}{m^2 K}]$
Enthalpy of vaporization $h_{vap}$	$4419.1 [\frac{J}{kg K}]$

### 4.3.4 Boiling curve diagram

In (Ahmad et al., 2016) a NRTL activity coefficient was derived in Aspen Plus from the existing vapor-liquid equilibrium of the [DBNH][OAc]-H<sub>2</sub>O binary. In the Comsol model the boiling curve (for  $p = 15$  mbar) was used as a function of the water content  $x_1$  to determine the saturation temperature.

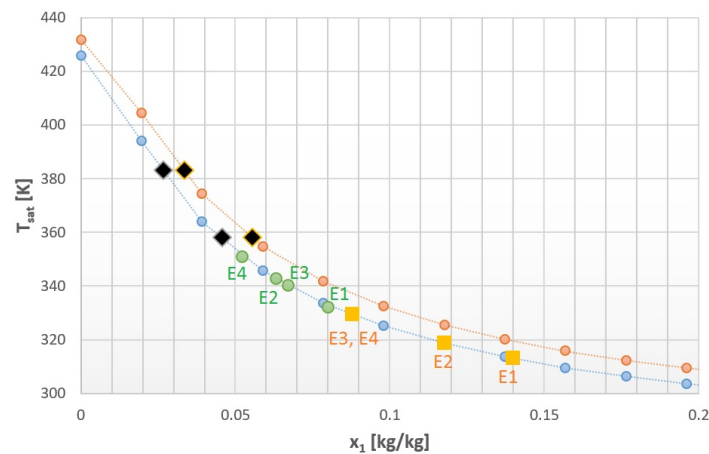


Figure 4.10: Boiling curves ( $T$ - $x$  diagram) at 20 mbar (orange) and 15 mbar (blue). The dots and squares mark different experimental values. Green  $\theta_{sat} = \theta_r$ , orange  $\theta_{sat} = \theta_{sat}(x_{1,r})$

In figure (4.10) the yellow dots mark the corresponding temperature for the residue concentration. Taking the measured residue temperature the green dots yield the respective values of the corresponding mass fractions from the boiling curve.

The black dots mark the mass fractions that would result from the heating jacket temperature, which was set for 85 °C (E1, E3) and 110 °C (E2 and E4).

The evaporation runs in Ahmad et al. (2016) were run at 20 mbar and 80-85 °C. There  $x_1$  was between 0.05 and 0.1.

### 4.3.5 Results of the $COM_{IL/H_2O}$ model

In Comsol a number of ideal stages were simulated. The values for the saturation temperature (BC at lines 3,5,7 see figure 4.5) were taken from the data available from Aspen Plus (section 4.3.4). The resulting material parameters (film thickness, heat conductivity and viscosity ) and the heat flux at the interface were calculated. For one single stage the procedure was as following:

$$F_i = F_0 \frac{x_{1,i}}{x_{1,0}} \quad (4.3.3)$$

Then the saturation temperature was set on the basis of a given  $\dot{F}$  and  $x_1$  and the simulation of the respective ideal stage started. For each stage the evaporating heat flux ( $\dot{q}_e$ ), wall temperature and material parameters ( $\delta_f, \mu, \lambda$ ) were noted down (see table 4.7) yielding a function of discrete points, which were interpolated linearly (4 points between each stage. For example between  $x_1 = 82.4 \%$  and  $x_1 = 76.5 \%$ ):

$$a_i = a_{i-1} + \frac{a_{exp,i-1} - a_{exp,i}}{5} \quad (4.3.4)$$

From the known heat flux, enthalpy of evaporation, evaporator circumference and stage feed-rate the theoretical height  $H_i$  of that stage was calculated for every model- ( $a_{exp,i}$ ) and interpolated value ( $a_i$ ):

$$H_{i,th} = \frac{\dot{F}_i x_{1,i} - \dot{F}_{i+1} x_{1,i+1}}{\dot{m}_{i,e}} \quad (4.3.5)$$

$$\dot{m}_{i,e} = \frac{\dot{q}_{mod,i} \pi d_e}{h_{vap}}$$

The water content difference  $\Delta x_1$  between each point (model and interpolated) was approximately 1 %. Each one was assumed to be an ideal stage. In the case of E1 this resulted in 70 ideal stages to reach a residue water content of 14.10 %. The experimentally determined water content of the residue  $x_{1,r}$  defined the last stage of the modeled stage column. The



Table 4.7: calculated heat flux and evaporation mass flux  $\dot{m}_e$  for different  $x_1$ , simulation E1

Modeled stage	$x_{1,i}$ [ $\frac{kg}{kg}$ ]	$\dot{F}_i$ [ $\frac{kg}{h}$ ]	$\theta_{sat,i}$ [ $^{\circ}C$ ]	$\dot{q}_{mod,i}$ [ $\frac{kW}{m^2}$ ]	$\dot{m}_{e,i}$ [ $10^{-3}\frac{kg}{s}$ ]
1	82.4 %	3.60	13.4	24.2	9.88
2	76.5 %	3.34	13.7	22.3	9.11
3	70.6 %	3.09	14.0	20.8	8.47
4	64.7 %	2.83	14.4	19.3	7.86
5	60.8 %	2,66	14.7	18.2	7.41
6	54.9 %	2.40	15.3	19.1	7.19
7	51.0 %	2.23	15.8	18.2	6.92
8	45.1 %	1.97	16.9	17.6	6.76
9	41.2 %	1.80	17.8	17.0	7.19
10	35.3 %	1.54	19.6	16.6	6.76
11	29.4 %	1.29	22.3	15.7	6.40
12	25.5 %	1.11	24.8	15.5	6.31
13	19.6 %	0.86	30.5	15.0	6.11
14	15.7 %	0.69	36.5	14.4	5.85
15	11.8 %	0.51	45.5	12.9	5.26
16	9.8 %	0.43	52.0	11.4	4.65
17	7.8 %	0.34	60.6	9.0	3.67

sum of the single stages yielded the total theoretical height of the evaporator:

$$H_{th} = \sum_{i=1}^k H_{i,th} \quad (4.3.6)$$

Table (4.8) compares the theoretical values of the model with the experiments:

The model shows good accordance with E1, all the other results predict a more efficient evaporation in the model as the theoretical total height is smaller than the actual

## 4 Models

Table 4.8: Theoretical lengths of the model in comparison with experimental results.

	E1	E2	E3	E4
$H_{th}$	266.7 mm	176.9 mm	119.0 mm	90.5 mm
$H_e$	262 mm	262 mm	262 mm	262 mm
$x_1$ at $z=262$ mm	16.9 %	2.9 %	5.2 %	2.9 %
$x_1 \neq x_{1,r}$ <sup>3</sup>		$(\theta_{sat} = \theta_h)$ <sup>4</sup>	$(\theta_{sat} = \theta_h)$ <sup>4</sup>	$(\theta_{sat} = \theta_h)$ <sup>4</sup>
$x_{1,r}$	14.1 %	11.8 %	8.8 %	8.6 %

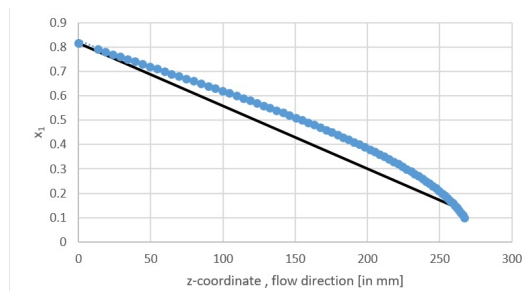


Figure 4.11: total theoretical height (blue) as function of  $x_1$   
exp. E1

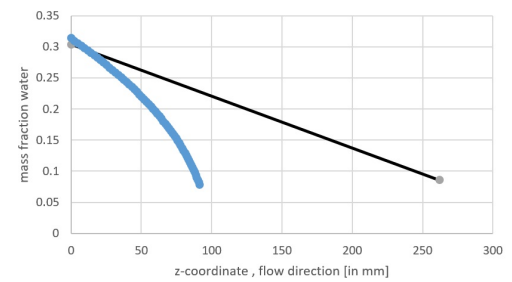


Figure 4.12: total theoretical height (blue) as function of  $x_1$   
exp. E4

evaporator height ( $H_e = 262mm$ ).

An overall mass balance (assuming  $\frac{c_p \Delta T}{h_{vap}} \ll 1$ ) of the experimental values yield lower heat fluxes than the predicted model (see table 4.9):

$$\dot{q}_{exp} = \frac{\dot{F} \zeta_d h_{vap}}{A_{evp}} \quad (4.3.7)$$

The average value of the model heat flux ( $\bar{q}_e$ ) and film thickness ( $\bar{\delta}_f$ ) was determined by the average over all stages:

$$\bar{q}_e = \frac{\sum_{i=1}^k \dot{q}_{i,e}}{k} \quad (4.3.8)$$

<sup>3</sup>The number of ideal stages was determined by the actual evaporator height instead of the experimental residue water content  $x_{1,r}$ .

<sup>4</sup>The theoretical height of the last stage is infinite as the saturation temperature is equal to the heating jacket temperature

Table 4.9: Comparison of the averaged model heat flux and experimental heat flux

	E1	E2	E3	E4
$\dot{q}_{exp} [\frac{kW}{m^2}]$	16.0	16.5	4.1	5.2
$\bar{q}_e [\frac{kW}{m^2}]$	16.8	26.60	11.3	19.9
$avg(\theta_w - \theta_{sat}) [K]$	28.2	43.2	26.2	45.3
$\bar{\delta}_f [mm]$	0.28	0.25	0.25	0.26

## Parameter profiles

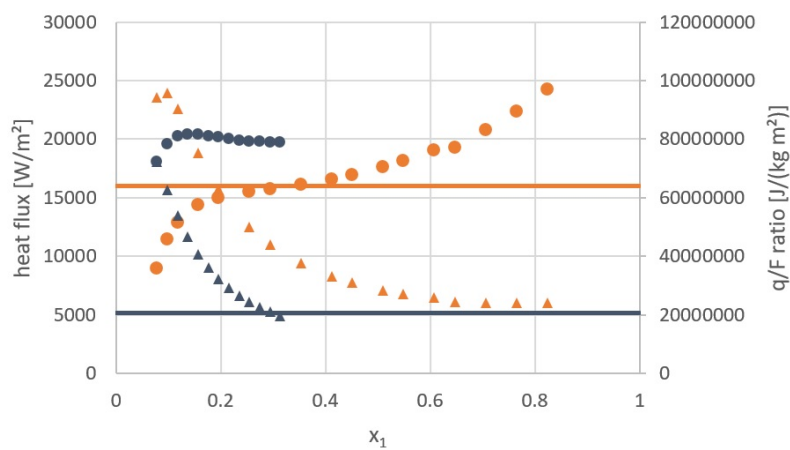


Figure 4.13:  $\dot{q}_e$  (dots),  $\frac{\dot{q}_e}{F}$  (triangles) and  $\bar{q}_{exp} = const$  (lines) of E1 (orange) and E4 (blue) in comparison

Figure 4.13 shows the heat flux and heat flux feed ratio ( $\frac{\dot{q}_e}{F}$ ) as functions of the mass fraction  $x_1$ . The heat flux in E1 is decreasing with increasing mass fraction, the increasing temperature of the saturation point is the determining factor reducing the temperature difference between the heating jacket and the fluid.

In E4  $\dot{q}$  reaches a maximum value at  $x_1 = 13\%$ . Until that point the slightly

#### 4 Models

decreasing film thickness and heat conductivity (since the saturation temperature is set as a boundary condition) might be reasons for the increasing heat flux.

The heat flux feed ratio puts the occurring evaporation into relation with the remaining liquid to be evaporated. For E1 it increases until  $x_1 = 9.8\%$ .

The lines in figure show the deviation of the heat flux to the averaged experimental heat flux. E1 is close to the experimental value, whereas E4 is significantly higher than its experimental flux.

### Thermal resistances

As the experimental results of the overall heat transfer coefficient lie in a range of 200-500  $\frac{W}{m^2 K}$  a rough estimate indicates the main resistance to be in the heating jacket.

The evaporator manufacturers UIC GmbH specified the material and thickness of the steel wall between the evaporator and heating jacket:

Table 4.10: Specifications of the wall between the evaporator and the heating jacket

Material	Steel EN 10020 - 1.4571 (X6CrNiMoTi17-12-2)
$\lambda_w \left[ \frac{W}{m K} \right]$	15
$s_w \left[ mm \right]$	3.6
$\alpha_w = \frac{\lambda_w}{s_w} \left[ \frac{W}{m^2 K} \right]$	4167

For the falling film one optimistic (water, thin film) and one conservative (ionic liquid, thick film) estimation were made:

The steel wall and a liquid aqueous film are clearly above the overall heat transfer coefficient making the heating medium the main thermal resistance of the evaporation.

In the case of pure ionic liquid the falling film possesses a similar heat transfer coefficient as the heating jacket. If even distribution of the feed cannot be assumed, a thicker

Table 4.11: Specifications of the liquid film

	Optimistic	Conservative
$\lambda_f$ [ $\frac{W}{mK}$ ]	0.591	0.1
$\delta_f$ [mm]	0.1	0.4
$\alpha_f = \frac{\lambda_w}{\delta_w}$ [ $\frac{W}{m^2K}$ ]	5910	250

film could lower the heat transfer coefficient of the film significantly.

### Change of material parameters along the evaporator height

The heat flux (figure 4.13) did not decrease until very low water contents. Although the heat conductivity is decreasing, the viscosity (see Appendix) decreases as a result of the higher boiling temperature, which is the determining factor for the heat flux in the model.

In E1 and E2 there is a slight increase of  $\delta_f$  from 0.33 mm to 0.36 mm after which the film start decreasing due to the relatively higher amount of liquid evaporating and decreasing viscosity due to higher saturation temperatures. The ratio of heat flux to feed rate show that the decreasing film flow overweight the declining temperature difference ( $\theta_h - \theta_{sat}$ ) until very low water contents ( $x_1 \sim 5-7\%$ ) (see figure 4.13).

### 4.3.6 Assessment calculations

As the predictions of the  $COM_{IL/H_2O}$  model were too optimistic in comparison to the experimental results, different parameters were put into relation with design calculations of the evaporator.

First an effective surface area was derived with a correction factor  $f_{cor,A}$  to level out the differences between the experimental and modeled heat flux.

In a second calculation a logarithmic temperature difference for the heating jacket

#### 4 Models

was assumed. The overall heat transfer coefficient of the evaporator  $\alpha_{model}$  was calculated and for the given experimental heat flux  $\dot{q}_{exp}$  the logarithmic temperature difference was solved for the leaving temperature of the heating medium  $\theta_{h,d}$ . The same calculation was made for the experimental overall heat transfer coefficient  $\alpha_{exp}$ .

### Theoretical surface area

The theoretical surface area required to have the same heat rate ( $\dot{Q}$ ) with different heat fluxes was calculated:

$$A_{th} = \frac{\dot{F}(x_{1,F} - x_{1,r})}{h_{vap} \bar{q}_e} = \frac{\dot{q}_{exp}}{\bar{q}_e A_e} \quad (4.3.9)$$

Table 4.12: Calculation of the theoretically required surface area  $A_{th}$

	E1	E2	E3	E4
$\bar{q}_{exp} [\frac{kW}{m^2}]$	16.0	16.5	4.1	5.2
$\bar{q}_e [\frac{kW}{m^2}]$	16.8	26.60	11.3	19.9
$f_{cor,A} = \frac{A_{th}}{A_e} [\frac{m^2}{m^2}]$	95.4 %	62.0 %	36.3 %	26.0 %

Every experiment was conducted with the same feed rate, E1 and E2 had the same feed material properties, therefore the hydrodynamic behavior should not change. However, there would be a significant change in the wetted surface area, if a change in the flow type was the reason for the smaller contact area.

### Mean logarithmic temperature difference model values

The average values of the film thickness and heat conductivity of all single equilibrium stages were calculated (in analogy to equation 4.3.8) and the overall heat transfer coefficient of the model was derived:

$$\alpha_{model} = \left( \frac{1}{\alpha_h} + \frac{1}{\alpha_f} \right)^{-1} = \left( \frac{1}{\alpha_{oil}} + \frac{s_w}{\lambda_w} + \frac{\bar{\delta}_f}{\lambda_f} \right)^{-1} \quad (4.3.10)$$

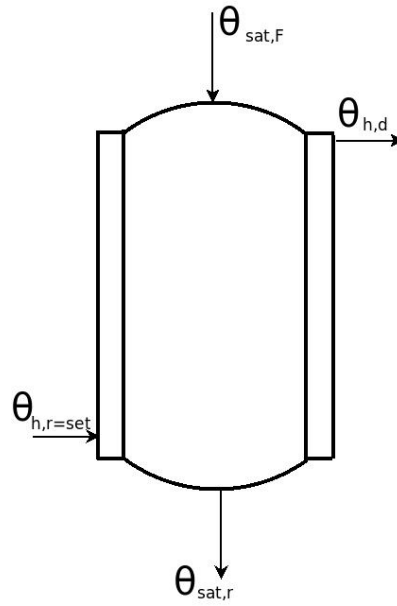


Figure 4.14: counter current heat exchanger with inlet and outlet temperatures

In table (4.13)  $\alpha_h$  is split up into the heat transfer coefficient of the medium ( $\alpha_{oil}$ ) and the wall ( $\alpha_w$ ) to allow a comparison of the single thermal resistances. The overall heat flux is the product of the overall heat transfer coefficient and mean logarithmic temperature difference for which the system was solved:

$$\Delta T_{ln} = \frac{q_{exp}}{\alpha_{model}} \quad (4.3.11)$$

$$\Delta T_{ln} = \frac{(\theta_{h,set} - \theta_{sat,r}) - (\theta_{h,d} - \theta_{sat,d})}{\ln\left(\frac{\theta_{h,set} - \theta_r}{\theta_{h,d} - \theta_{sat,d}}\right)}$$

According to the plant drawings the heating jacket works as a counter-current exchanger. Therefore the temperature difference at the bottom of the evaporator was assumed to be  $\theta_{h,set} - \theta_{sat,r}$ , whereas the temperature difference at the top was unknown  $\theta_{h,d} - \theta_{sat,F}$ . For the liquid film in the evaporator the respective boiling temperatures of the residue ( $\theta_{sat,r}$ ) and the feed ( $\theta_{sat,F}$ ) were assumed. The only remaining unknown parameter is  $\theta_{h,d}$  for which the system was solved.

These results are implausible in terms of energy consumption. If there was really a temperature gradient in the heating medium, then it should be proportional to the consumed

## 4 Models

Table 4.13: resulting  $\Delta T_{ln}$  for the overall heat transfer coefficient of the model

	E1	E2	E3	E4
$\Delta T_{ln} [K]$	57.0	51.7	16.7	19.7
$\alpha_{model} [\frac{W}{m^2 K}]$	779	439	262	182
$\bar{\delta}_f [mm]$	0.28	0.25	0.11	0.12
$\bar{\lambda}_f [\frac{W}{m K}]$	0.17	0.16	0.11	0.12
$\alpha_{oil} [\frac{W}{m^2 K}]$	595	736	595	736
$\alpha_w [\frac{W}{m^2 K}]$	4167	4167	4167	4167
$\alpha_f [\frac{W}{m^2 K}]$	608	651	464	449
$\bar{q}_e [\frac{kW}{m^2}]$	16.8	26.60	11.3	19.9

Table 4.14: resulting  $\theta_{h,d}$  for given  $\Delta T_{ln}$

	E1	E2	E3	E4
$\Delta T_{ln} [K]$	57.0	51.7	16.7	19.7
$\theta_{h,d} [^{\circ}C]$	84.6	54.1	33.3	54.0
$\theta_{h,set} [^{\circ}C]$	85	110	85	110

energy. E1 and E2 have higher evaporation rates than E3 and E4, but the resulting value of  $\theta_{h,d}$  is closer to the Set point value of the heating jacket.

### Mean logarithmic temperature difference experimental values

In the same manner as for  $\alpha_{model}$ , the mean logarithmic temperature differences for  $\alpha_{exp}$  were calculated according to equation 4.3.11 and  $\Delta T_{ln}$  solved for  $\theta_{h,d}$

E4 is the only experiment, where the heating jacket temperature does not vary for the assumed logarithmic temperature difference. Whereas  $\theta_{h,d}$  is similar for E1 and E4, the derived values of E2 and E4 are not.



Table 4.15: resulting  $\Delta T_{ln}$  and  $\theta_{h,d}$  for  $\alpha_{exp}$ 

	E1	E2	E3	E4
$\Delta T_{ln}$ [K]	36.5	53.0	21.7	34.4
$\alpha_{exp}$ [ $\frac{W}{m^2 K}$ ]	438	311	189	150
$\bar{q}_e$ [ $\frac{kW}{m^2}$ ]	16.8	26.60	11.3	19.9
$\theta_{h,d}$ [ $^{\circ}C$ ]	42.7	56.4	40.5	101
$\theta_{h,set}$ [ $^{\circ}C$ ]	85	110	85	110

## 4.4 Conclusions

The comparison of the derived required length to the actual length indicates a too optimistic prediction. The specified boundary conditions of the heat transfer, saturation point at the liquid-vapor interface and constant heating jacket temperature lead to very high temperature differences of 20 - 30 K for a film thickness of 0.1-0.4 mm.

As the heat transfer coefficient was determined as a function for several water thin-film evaporation cases, the gap between model and experiments cannot be corrected by a new arbitrary heat transfer function in the case of ionic liquid separation. Also the difference of the experimental overall heat transfer coefficient  $\alpha_{E1,exp} = 438 \frac{W}{m^2 K}$  and  $\alpha_{E3,exp} = 189 \frac{W}{m^2 K}$  shows an unexpected deviation.

Both experiments were conducted at the same feed rate, heating jacket temperature and pressure. The only difference was the initial concentration of ionic liquid leading to different saturation temperatures and thermal profiles in the evaporator. The latter could provide possibly an explanation for the difference, since a mean logarithmic temperature difference was used to derive the heat transfer coefficient in the case of ionic liquid purification.

The model assumes that only water is evaporating, although the experimental results show especially for E4 that partially also components of the ionic liquid are in the distillate (see Appendix). The chemical reactions responsible for the thermal decomposing of the ionic

#### 4 Models

liquid lead to more volatile components that evaporate more easily. However, this process phenomenon was left out in the modeling.

In the cases of E3 and E4 the lower heat conductivity due to lower  $x_1$  could be a possible reason for the deviation if the actual flow was different to a falling film flow. The experimental results of E1 and E2 showed only a minimal improvement of the heat flux  $\bar{q}_e$  from  $16.0 \frac{kW}{m^2}$  to  $16.5 \frac{kW}{m^2}$ , despite the temperature change of the heating jacket from 85 to 110 °C. In the model this led to a significant change of the residual water content.

The model is calculating the heat flux for different thermodynamic stages, assuming equilibrium as in the Gröpp and Schlünder or Billet theory. Diffusion and concentration gradients are neglected. The determining parameters for the evaporation are hence the radial heat flux and enthalpy of vaporization that is assumed constant.

As the only theory available, the Nusselt theory was used to derive a uniform film thickness, assuming the wipers to distribute the feed ideally over the evaporator surface. The manufacturers of the evaporator, UIC, stated the film thickness to be in between 0.1 and 1.5 mm. Values of the model lied in between 0.1 and 0.4 mm for the IL-H<sub>2</sub>O evaporation. For the water model the film thickness was around 0.1 mm. In comparison to the existing literature on falling film and wiped film evaporation, the considered ionic liquid purification process operates at very low feed rates and with very high separation factors.

The experimental heat transfer coefficients were calculated from the energy balance and the geometry of the evaporator, assuming that the liquid is wetting the whole surface area of the wall. However, this led to significantly different values.

In the case of water evaporation it varied from 358 to  $493 \frac{W}{m^2 K}$  for a wide operating range. The temperature dependent viscosity of the heating oil was not considered in the model, a linear function was used instead of a constant heat transfer coefficient.

In the case of ionic liquid separation the experimental heat transfer coefficients varied from 150 (E4) to  $438 \frac{W}{m^2 K}$  (E1) (table 3.11). In E4, the heating jacket temperature was set at 110 °C, which would imply an enhanced heat transfer. However, the heat transfer coefficient

is lower than the lowest value of the water evaporations.

The higher temperature should enhance the heat transfer from the heating jacket to the evaporating film,  $\alpha_h$ . However, the overall coefficient was decreasing. To identify a possible missing link between the model and experiments, calculations were made to establish a possible correcting factor between the evaporator surface and an effective, wetted surface. The derived results still could not explain the decreasing  $\alpha_{exp}$ .

No particular reason was found in the assessment calculations. It can be said that the model assumes a state of equilibrium, which does not coincide with the given experimental results provided for the thesis. However, in (Ahmad et al., 2016) single stage flash models with assumed thermodynamic equilibrium showed an approximate good accordance with the experimental data provided for that paper.



## 5 Outlook

The existing model for the ionic liquid purification predicted the evaporation of a series of single ideal stages instead of a continuous thin-film flow. The objective of a CFD model must be a model that describes fully the hydrodynamic behavior of the flow including the liquid film – vapor interface. This requires a correct two-phase model with source terms for local evaporation and condensation conditions as functions of the temperature, heat flux and concentration. In (Kharangate and Mudawar, 2017) a few references were made to similar CFD-cases and suitable evaporation modeling methods.

It is evident that such a kind of model needs detailed information on the considered process. On the one hand, the experimental research has to be extended to obtain more reliable results. On the other hand, consistent models on a simpler level have to be designed to provide a reference model for CFD simulations.

The heat transfer is yet not fully understood. Both experimental and model values of the heat transfer coefficient varied in a wide range. The heat transfer coefficient should be estimated on the basis of experimental results and a simple valid equation for the energy balance set for which that coefficient would predict the evaporation rate correctly. In the CFD model that constant should be only a parameter of a boundary condition for the resulting heat transfer of the solver.

In (Ahmad et al., 2016), the ionic liquid was separated more efficiently, although the evaporator was operated at a lower temperature and higher pressure than the experiments discussed in this thesis. In consequence, the experiments of the ionic liquid purification should be repeated to achieve a certain reliability. The experiments of this thesis were run for a total time of 30 minutes. The resulting water contents of the residue were higher than in (Ahmad

## 5 Outlook

et al., 2016). One possible reason for the deviation could be a transition time affecting the final residue concentrations before reaching steady state conditions. The residue was only measured at the end of every experiment. In future tests the residue should be checked for transient changes. Also the impact of the pre-heater and residue heater should be analyzed. In the mentioned Aspen plus models only the heating jacket was considered as the main energy provider for the evaporation.

As mentioned before, it would be practical to create models on a lower description level than CFD models. A simpler model, i.e. a MATLAB code for heat transfer over an immobile thin liquid layer, is easier to check on wrong assumptions than a CFD case. In this thesis the particular reasons for the inaccurate prediction of the process could not be defined exactly. Possibly the general assumption of equilibrium conditions is not correct after all.

The current model does not consider the chemical reactions of [DBNH][OAc] that lead to more volatile products and overall loss of the ionic liquid in the process. In a next step, after a working description of the thermal conditions within the evaporator the reactions could be considered as functions of the temperature and velocity flow to predict thermal degradation of the ionic liquid.

This model could deliver needed information for the Aspen plus models in (Ahmad et al., 2016), (Ilmanen, 2017) to provide realistic values for the input parameters as the temperature or heat flux.

The literature study gave an overview of the existing research available on wiped film and falling film evaporation. The Nusselt correlation (equation 1.3.1) is of limited practical use in the case of the ionic liquid purification due to the very small range of parameters. The very small feed rate ( $Re_f < 10$ ) far off the transition region to the turbulent flow ( $Re_f < 400$ ). However, the actual feed rate limit in a wiped film is unknown. At a certain point liquid accumulates in the bow wave that is heated less than the falling liquid at the wall.

Regarding CFD modeling in OpenFoam or Fluent, a broad literature treating evaporation in CFD modeling exists. This knowledge could be used to create a COMSOL model with occurring evaporation in a two phase flow. However, the required time to develop and

validate such models should be compared to its use – are detailed information on the flow really necessary for a scale-up of the process or could be achieved the same with experimental research in less time and effort? Also a very detailed model approach requires information of certain parameters as the residence distribution time, reaction constants, actual film thickness or bow waves.

All in all, this work provides numbers and figures for the process development. Although certain values are varying, above all the heat transfer coefficient, they give an idea in which range the thin-film evaporator operates. For many areas (scale-up, experiments, modeling) the existing data gives a first guess on the precision of the experiments and the models or the needed evaporation rate. Also certain key process parameters were identified and assumptions discarded. s





# Bibliography

- Aalto. Aalto school of chemical technology, course slides engineering thermodynamics, separation processes part 1, activity coefficient models, p.20, 2016.
- Abichandani, H. and Sarma, S. Heat transfer and power requirements in horizontal thin film scraped surface heat exchangers. *Chemical Engineering Science*, 43(4):871–881, 1988a. doi: 10.1016/0009-2509(88)80083-6. URL <https://doi.org/10.1016%2F0009-2509%2888%2980083-6>.
- Abichandani, H. and Sarma, S. Evaporation in a horizontal thin film scraped surface heat exchanger. *Journal of Food Process Engineering*, 14(3):173–187, 1988b. doi: 10.1111/j.1745-4530.1991.tb00089.x. URL <http://dx.doi.org/10.1111/j.1745-4530.1991.tb00089.x>.
- Ahmad, W., Ostonen, A., Jakobsson, K., Uusi-Kyyny, P., Alopaeus, V., Hyväkkö, U., and King, A. W. Feasibility of thermal separation in recycling of the distillable ionic liquid [DBNH][OAc] in cellulose fiber production. *Chemical Engineering Research and Design*, 114:287–298, oct 2016. doi: 10.1016/j.cherd.2016.08.032. URL <https://doi.org/10.1016%2Fj.cherd.2016.08.032>.
- Al-Najem, N., Ezuddin, K., and Darwish, M. Heat transfer analysis of preheated turbulent falling films in vertical tube evaporators. *Desalination*, 115(1):43–55, mar 1998. doi: 10.1016/s0011-9164(98)00025-3. URL <https://doi.org/10.1016%2Fs0011-9164%2898%2900025-3>.
- Albert, J. and Mueller, K. Thermal conductivity of ionic liquids: An estimation approach. *Chemical Engineering Science*, 119:109–113, 2014. URL <https://doi.org/10.1016/j.ces.2014.08.023>.

## Bibliography

- Andersen, M. A interphasechangeFoam tutorial, November 2011. URL [http://www.tfd.chalmers.se/~hani/kurser/OS\\_CFD\\_2011/MartinAndersen/Tutorial\\_interPhaseChangeFoam.pdf](http://www.tfd.chalmers.se/~hani/kurser/OS_CFD_2011/MartinAndersen/Tutorial_interPhaseChangeFoam.pdf).
- Bott, T. R. and Romero, J. J. B. Heat transfer across a scraped surface. *The Canadian Journal of Chemical Engineering*, 41(5):213–219, oct 1963. doi: 10.1002/cjce.5450410506. URL <https://doi.org/10.1002/cjce.5450410506>.
- Burkhart, F. Recycling of the solvent from the spinbath. Master's thesis, Aalto school of chemical technology, Finland, 2016.
- CFDDirect. Openfoam user guide: 2 tutorials, a. URL <https://cfd.direct/openfoam/user-guide/tutorials/>.
- CFDDirect. Openfoam structure, b. URL <https://cdn.cfd.direct/docs/user-guide/img/user0x.png>.
- CFDDirect. Boundaries, July 2017. URL <https://cfd.direct/openfoam/user-guide/boundaries/>.
- Chang, H.-C. Wave evolution on a falling film. *Annual Review of Fluid Mechanics*, 26:103–136, 1994.
- Comsol. Comsol multiphysics, a. URL <https://www.comsol.com/comsol-multiphysics>.
- Comsol. Gui comsol, b. URL <https://cdn.comsol.com/release/44/general/comsolmulti/heat-exchanger-window.png>.
- Dietze, G. F. and Kneer, R. Capillary flow separation in 2- and 3-dimensional laminar falling liquid films. In *2010 14th International Heat Transfer Conference, Volume 3*. ASME, 2010. doi: 10.1115/ihtc14-22064. URL <https://doi.org/10.1115/ihtc14-22064>.
- DIPPR. Dippr project 801, 2015.
- Dziak, J. Mass and heat transfer during thin-film evaporation of liquid solutions. In *Advanced Topics in Mass Transfer*. InTech, feb 2011. doi: 10.5772/14970. URL <https://doi.org/10.5772/14970>.

10.5772%2F14970.

- E.Minton, P. *Handbook of evaporation technology*, pages 5, 70. William Andrew Publishing/Noyes, New Jersey, 1986.
- Eslami, M. R. Elements and local coordinates. In *Finite Elements Methods in Mechanics*, pages 57–77. Springer International Publishing, 2014. doi: 10.1007/978-3-319-08037-6\_4. URL [https://doi.org/10.1007%2F978-3-319-08037-6\\_4](https://doi.org/10.1007%2F978-3-319-08037-6_4).
- Ferziger, J. H. and Perić, M. *Interpolation and Differentiation Practices*, pages 76–81. Springer Berlin Heidelberg, 2002. doi: 10.1007/978-3-642-56026-2. URL <https://doi.org/10.1007%2F978-3-642-56026-2>.
- Fletcher, C. Finite element method and interpolation. In *Computational Techniques for Fluid Dynamics 1*, pages 111–112. Springer Berlin Heidelberg, 1997. doi: 10.1007/978-3-642-58229-5\_5. URL [https://doi.org/10.1007%2F978-3-642-58229-5\\_5](https://doi.org/10.1007%2F978-3-642-58229-5_5).
- Fontoura, N., Matos. A three-dimensional two-phase flow model with phase change inside a tube of petrochemical pre-heaters. *Fuel*, 110:196–203, 2013. URL <https://doi.org/10.1016/j.fuel.2012.09.065>.
- Fujikawa, S., Yano, T., and Watanabe, M. Significance of molecular and fluid-dynamic approaches to interface phenomena. In *Heat and Mass Transfer*, pages 1–17. Springer Berlin Heidelberg, 2011. doi: 10.1007/978-3-642-18038-5\_1. URL [https://doi.org/10.1007%2F978-3-642-18038-5\\_1](https://doi.org/10.1007%2F978-3-642-18038-5_1).
- Glover, W. B. Selecting evaporators for process applications. *Chemical Engineering Process*, 100:26–33, 2004 2004.
- Gourdon, M., Karlsson, E., Innings, F., Jongasma, A., and Vamling, L. Heat transfer for falling film evaporation of industrially relevant fluids up to very high prandtl numbers. *Heat and Mass Transfer*, 52(2):379–391, apr 2015. doi: 10.1007/s00231-015-1556-9. URL <https://doi.org/10.1007%2Fs00231-015-1556-9>.
- Gropp, U. and Schlünder, E. The influence of liquid-side mass transfer on heat transfer and

## Bibliography

- selectivity during surface and nucleate boiling of liquid mixtures in a falling film. *Chemical Engineering and Processing: Process Intensification*, 20(2):103–114, mar 1986. doi: 10.1016/0255-2701(86)85014-0. URL <https://doi.org/10.1016%2F0255-2701%2886%2985014-0>.
- Haider, J. Numerical modelling of evaporation and condensation phenomena. Master's thesis, University of stuttgart, 2013.
- Hardt, S. and F.Wondra. Evaporation model for interfacial flows based on a continuum-field representation of the source terms. *Journal of computational physics*, 227(11):5871–5895, May 2008.
- Hämmerle, F. M. The cellulose gap (the future of cellulose fibres). *Lenzinger Berichte 89*, 89: 12–21, 2011.
- Ilmanen, P. modeling of thin film evaporator for ionic liquid recycling. Master's thesis, Aalto university school of chemical engineering, 2017.
- Ishigai, S., Nakanisi, S., Takehara, M., and oyabu, Z. Hydrodynamics and heat transfer of vertical falling liquid films : Part 2. analysis by using heat transfer data. *Bulletin of JSME*, 17 (103):106–114, 1974. doi: 10.1299/jsme1958.17.106. URL <https://doi.org/10.1299%2Fjsme1958.17.106>.
- Jäynä, T. Numerical patterns of door codes in otaniemi. *Review of the reader's alertfulness*, pages 1991–2210, 2017.
- Kharangate, C. and Mudawar, I. Review of computational studies on boiling and condensation. *International Journal of Heat and Mass transfer*, 108:1164–1196, may 2017. doi: 10.1016/j.ijheatmasstransfer.2016.12.065.
- Kim, B. J., Sohn, B. H., and Jeong, S. Two-phase flow regimes for counter-current air-water flows in narrow rectangular channels. *KSME International Journal*, 15(7):941–950, jul 2001. doi: 10.1007/bf03185272. URL <https://doi.org/10.1007%2Fbf03185272>.
- Kuhlmann, H. *Erhaltungsgleichungen für reibungsfreie Fluide*, pages 70–71. Pearson studies,

2007.

lccorp. thin film evaporator. URL <http://lccorp.com/tfe.svg>.

Lopez-Toledo, J. *Heat and mass transfer characteristics of a wiped film evaporator*. PhD thesis, University of Texas, 2006.

Ltd, O. Openfoam - introduction. URL <http://www.openfoam.com/documentation/user-guide/userch1.php#x3-20001>.

Ludwig, W. and Dziak, J. Cfd modelling of a laminar film flow. *Chemical and Process Engineering*, 30:417–430, 2009.

Manzini, G., 2012. URL [http://arturo.imati.cnr.it/~marco/resources/GIF/cell-centered\\_grid-2.gif](http://arturo.imati.cnr.it/~marco/resources/GIF/cell-centered_grid-2.gif).

Mather, R. and Wardman, R. *Lyocell fibres*, page 402. The Royal Society of Chemistry, 2015. doi: 10.1093/acref/9780199651450.001.0001.

McKelvey, J. M. and Sharps, G. V. Fluid transport in thin film polymer processors. *Polymer Engineering and Science*, 19(9):651–659, jul 1979. doi: 10.1002/pen.760190908. URL <https://doi.org/10.1002/pen.760190908>.

McKenna, T. F. Design model of a wiped film evaporator. applications to the devolatilisation of polymer melts. *Chemical Engineering Science*, 50(3):453–467, feb 1995. doi: 10.1016/0009-2509(94)00257-r. URL [https://doi.org/10.1016/0009-2509\(94\)00257-r](https://doi.org/10.1016/0009-2509(94)00257-r).

Nielsen, C. H., Kiil, S., Thomsen, H. W., and Dam-Johansen, K. Mass transfer in wetted-wall columns: Correlations at high reynolds numbers. *Chemical Engineering Science*, 53(3):495–503, feb 1998. doi: 10.1016/s0009-2509(97)00320-5. URL [https://doi.org/10.1016/s0009-2509\(97\)00320-5](https://doi.org/10.1016/s0009-2509(97)00320-5).

Numrich, R. Heat transfer in turbulent falling films. *Chemical Engineering & Technology*, 18(3):171–177, jun 1995. doi: 10.1002/ceat.270180305. URL <https://doi.org/10.1002/ceat.270180305>.

## Bibliography

- Nusselt, W. *Die Oberflächenkondensation des Wasserdampfes*, volume 60. Zeitschrift des Vereins Deutsche Ingenieure, 1916.
- Openfoam. interphasechangeFoam.c file reference, 2016. URL [http://www.openfoam.com/documentation/cpp-guide/html/interPhaseChangeFoam\\_8C.html](http://www.openfoam.com/documentation/cpp-guide/html/interPhaseChangeFoam_8C.html).
- Paraview. Overview paraview. URL <https://www.paraview.org/overview/>.
- Parviainen, A., King, A. W. T., Mutikainen, I., Hummel, M., Selg, C., Hauru, L. K. J., Sixta, H., and Kilpeläinen, I. Predicting cellulose solvating capabilities of acid-base conjugate ionic liquids. *ChemSusChem*, 6(11):2161–2169, sep 2013. doi: 10.1002/cssc.201300143. URL <https://doi.org/10.1002%2Fcssc.201300143>.
- Pawar, S., Mujumudar, A., and Thorat, B. Cfd analysis of flow pattern in the agitated thin film evaporator. *Chemical Engineering Research and Design*, 90(6):757–765, jun 2012. URL <http://dx.doi.org/10.1016/j.cherd.2011.09.017>.
- Pfennig, A., Schabel, W., and Wolf, H. D5 properties of multicomponent fluid mixtures. In *VDI Heat Atlas*, pages 513–550. Springer Berlin Heidelberg, 2010. doi: 10.1007/978-3-540-77877-6\_23. URL [https://doi.org/10.1007%2F978-3-540-77877-6\\_23](https://doi.org/10.1007%2F978-3-540-77877-6_23).
- Rusche, H. *Computational fluid dynamics of dispersed two-phase flows at high phase fractions*. PhD thesis, Imperial College of Science, Exhibition Road, London SW72BX, 12 2002.
- Schaschke, C. *viscose process*, page 402. Oxford university press, 2014. doi: 10.1093/acref/9780199651450.001.0001.
- Schmied, G. *Heat Transfer to Falling Films at Vertical*, pages 1287–1294. VDI, 2010.
- Schnabel and Schlünder. Heat transfer from vertical liquid films with or without evaporation. *Verfahrenstechnik*, 14:79–83, 1980.
- Schnabel, G. M3 heat transfer to falling films at vertical surfaces. In *VDI Heat Atlas*, pages 1287–1294. Springer Berlin Heidelberg, 2010. doi: 10.1007/978-3-540-77877-6\_96. URL [https://doi.org/10.1007%2F978-3-540-77877-6\\_96](https://doi.org/10.1007%2F978-3-540-77877-6_96).

- Schäfer, M. *Finite-Volume methods*, pages 78–79. Springer, 2006.
- Serth, R. W. and Lestina, T. G. Boiling heat transfer. In *Process Heat Transfer*, pages 317–360. Elsevier, 2014. doi: 10.1016/b978-0-12-397195-1.00009-1. URL <https://doi.org/10.1016%2Fb978-0-12-397195-1.00009-1>.
- Sinnott, R. *Vapour pressure*, page 330. Elsevier, 1999.
- Sixta. loncell-f: A high-strength regenerated cellulose fibre. *Nordic Pulp and Paper Research Journal*, 30(01):043–057, mar 2015. doi: 10.3183/npprj-2015-30-01-p043-057. URL <https://doi.org/10.3183%2Fnpprj-2015-30-01-p043-057>.
- SPX. Evaporator handbook.
- Therminol. Therminol 66. URL <https://www.therminol.com/products/Therminol-66>.
- Unterberg, W. and Edwards, D. K. Effect of dissolved solid on wiped-film evaporation. *Industrial & Engineering Chemistry Process Design and Development*, 6(3):268–276, jul 1967. doi: 10.1021/i260023a002. URL <https://doi.org/10.1021%2Fi260023a002>.
- Wassner, L. Wärmetechnische auslegung von fallfilmverdampfern. *Forschung im Ingenieurwesen*, 47(4):125–130, jul 1981. doi: 10.1007/bf02561082. URL <https://doi.org/10.1007%2Fbf02561082>.
- Won, Y. and Mills, A. Correlation of the effects of viscosity and surface tension on gas absorption rates into freely falling turbulent liquid films. *International Journal of Heat and Mass Transfer*, 25(2):223–229, feb 1982. doi: 10.1016/0017-9310(82)90008-4. URL <https://doi.org/10.1016%2F0017-9310%2882%2990008-4>.
- Zhou, S., Xi, X., and Sammakia, B. Modeling of boiling flow in microchannels for nucleation characteristics and performance optimization. *International Journal of Heat and Mass Transfer*, 64:706–718, sep 2013. URL <https://doi.org/10.1016/j.ijheatmasstransfer.2013.05.031>.
- Zienkewicz, O. *The finite element method: its basis and fundamentals*, chapter Weight residual methods, pages 57–59. Elsevier, 2005.

## *Bibliography*

Zienkiewicz, O. *The finite element method: its basis and fundamentals*, chapter Generalization of the finite element concepts, pages 54–56. Elsevier, 2005.

Zikanov, O. *Governing equations of fluid dynamics and heat transfer*, chapter Governing equations of fluid dynamics and heat transfer, pages 11–12. John Wiley & Sons, Incorporated, 2011.



# 6 Appendix

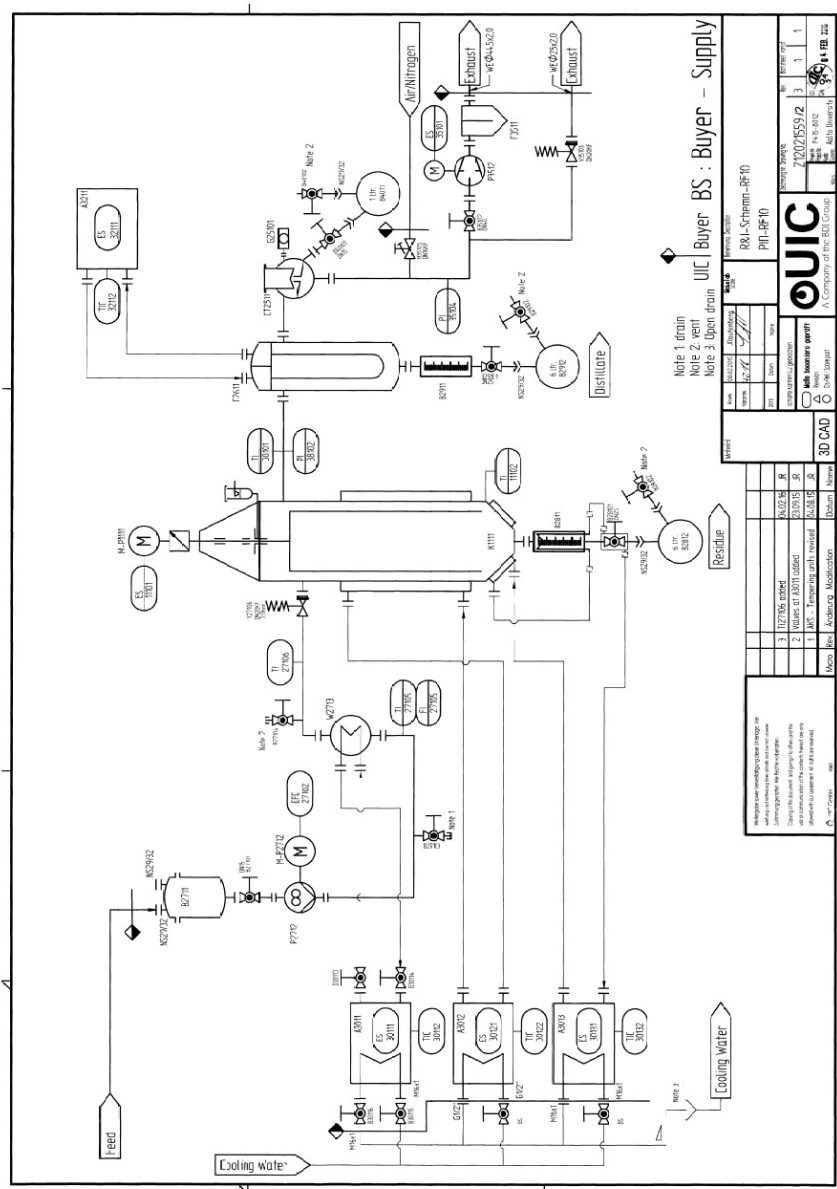


Figure 6.1: PID flowsheet of the evaporation plant

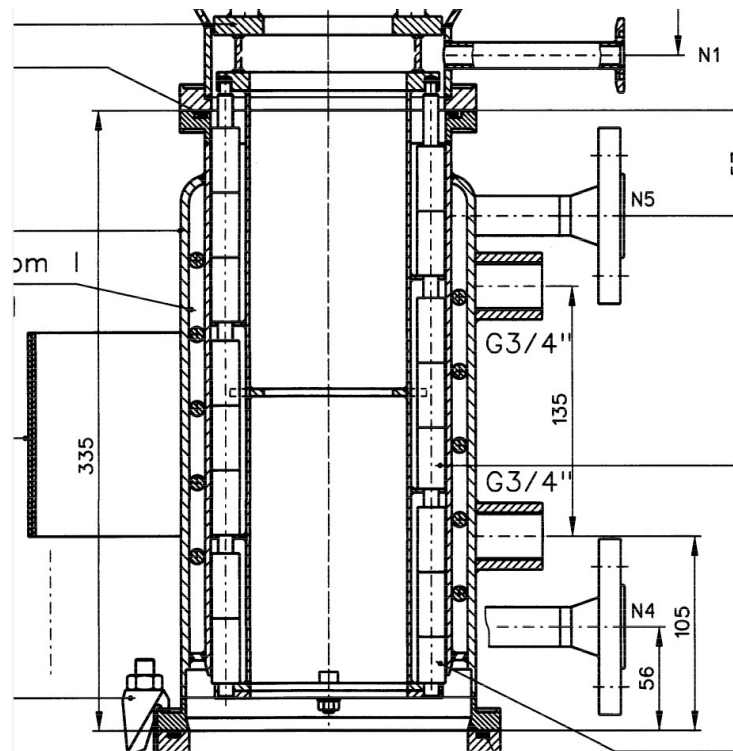


Figure 6.2: Extract of the assembly drawing of the thin-film evaporator. Inside the wiper basket the wiper blades are connected to a rotor

Table 6.1: Geometry dimensions of the thin-film evaporator

Evaporator height	$H_e$	262 mm
Wall thickness	$s_w$	3.5 mm
Diameter of wiper basket	$d_e$	126 mm
rotor diameter	$d_r$	111 mm
Gap between wall and wiper blade	$s_f$	2 mm
Operating range thin-film	$\delta_f^*$	0 -1.5 mm

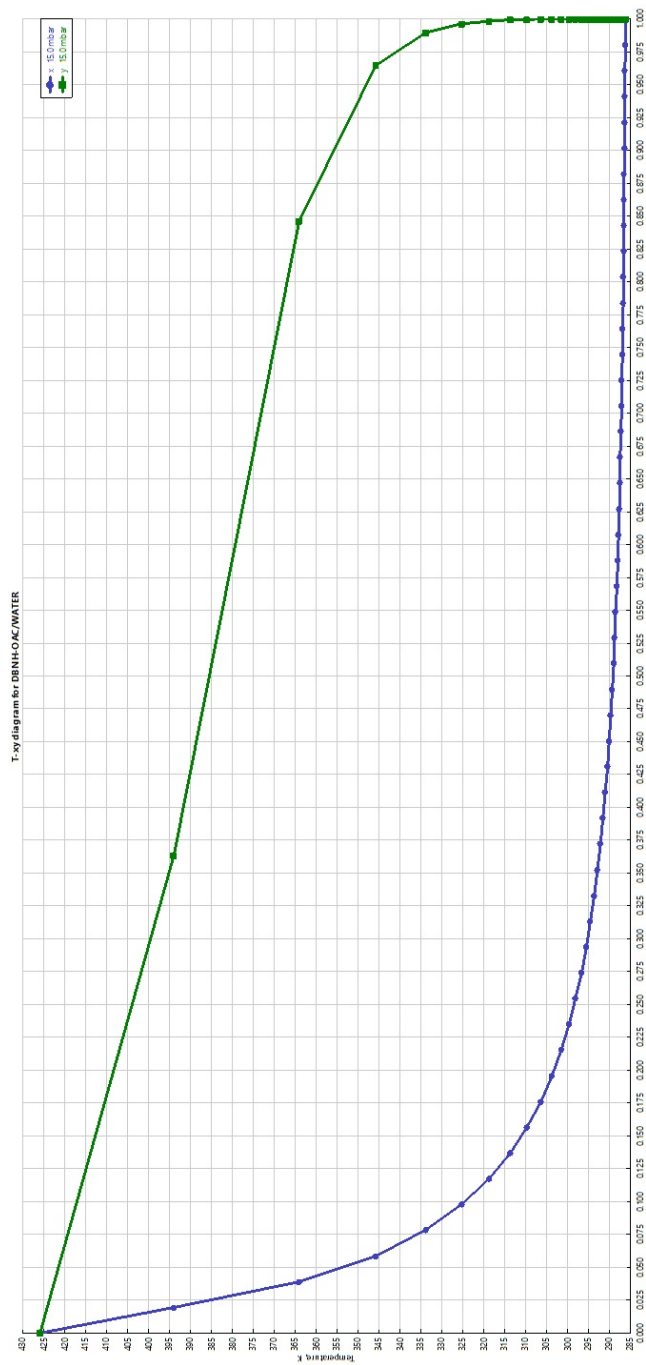


Figure 6.3: T-x,y phase diagram of the [DBNH][OAc]-H<sub>2</sub>O binary (Aspenplus, UNIQUAC)

## 6 Appendix

Table 6.2: Discrete model values E1

$\dot{F} [\frac{kg}{h}]$	$x_1 [\frac{kg}{kg}]$	$T_{sat} [K]$	$\delta_f [mm]$	$\lambda [\frac{W}{mK}]$	$\dot{m} [Pa s]$	$T_w [K]$	$\dot{q} [\frac{W}{m^2}]$	$\dot{m} [\frac{kg}{m^2 s}]$
3.60	82.35%	286.6	0.33	0.316	0.049	311.7	24224	0.0099
3.34	76.47%	286.8	0.34	0.274	0.065	315.4	22337	0.0091
3.09	70.59%	287.1	0.35	0.242	0.079	318.5	20776	0.0085
2.83	64.71%	287.5	0.36	0.216	0.092	321.4	19276	0.0079
2.66	60.78%	287.8	0.36	0.202	0.100	321.8	19079	0.0078
2.40	54.90%	288.5	0.36	0.184	0.111	323.6	18167	0.0074
2.23	50.98%	289.0	0.35	0.174	0.117	324.7	17641	0.0072
1.97	45.10%	290.0	0.34	0.160	0.123	326.0	16973	0.0069
1.80	41.18%	290.9	0.33	0.152	0.125	326.7	16592	0.0068
1.54	35.29%	292.8	0.31	0.142	0.124	327.7	16119	0.0066
1.29	29.41%	295.5	0.28	0.133	0.115	328.5	15710	0.0064
1.11	25.49%	298.0	0.26	0.127	0.105	329.0	15482	0.0063
0.86	19.61%	303.7	0.22	0.120	0.080	330.1	14986	0.0061
0.69	15.69%	309.6	0.18	0.115	0.060	331.5	14354	0.0059
0.51	11.76%	318.6	0.14	0.111	0.039	334.4	12912	0.0053
0.43	9.80%	325.1	0.12	0.109	0.030	337.3	11416	0.0047
0.34	7.84%	333.8	0.10	0.103	0.024	341.9	8992	0.0037

Table 6.3: Discrete model values E2

$\dot{F} [\frac{kg}{h}]$	$x_1 [\frac{kg}{kg}]$	$T_{sat} [K]$	$\delta_f [mm]$	$\lambda [\frac{W}{mK}]$	$\dot{m} [Pa s]$	$T_w [K]$	$\dot{q} [\frac{W}{m^2}]$	$\dot{m} [\frac{kg}{m^2 s}]$
3.60	82.35%	286.6	0.325	0.316	0.049	324.6	36939	0.01506
3.34	76.47%	286.8	0.344	0.274	0.065	329.4	34027	0.01387
3.09	70.59%	287.1	0.355	0.242	0.079	333.3	31626	0.01289
2.83	64.71%	287.5	0.359	0.216	0.092	336.5	29663	0.01209
2.66	60.78%	287.8	0.360	0.202	0.100	338.3	28548	0.01164
2.40	54.90%	288.5	0.356	0.184	0.111	340.6	27144	0.01107
2.23	50.98%	289.0	0.352	0.174	0.117	341.9	26359	0.01075
1.97	45.10%	290.0	0.340	0.160	0.123	343.5	25408	0.01036
1.80	41.18%	290.9	0.330	0.152	0.125	344.3	24905	0.01015
1.54	35.29%	292.8	0.309	0.142	0.124	345.2	24369	0.00993
1.29	29.41%	295.5	0.282	0.133	0.115	345.8	24056	0.00981
1.11	25.49%	298.0	0.258	0.127	0.105	345.9	24039	0.00980
0.86	19.61%	303.7	0.215	0.120	0.080	345.9	24109	0.00983
0.69	15.69%	309.6	0.180	0.115	0.060	346.1	24122	0.00983
0.51	11.76%	318.6	0.141	0.111	0.039	347.3	23599	0.00962
0.43	9.80%	325.1	0.122	0.109	0.030	349.1	22569	0.00920
0.34	7.84%	333.8	0.103	0.103	0.024	352.4	20608	0.00840
0.26	5.88%	345.8	0.084	0.105	0.017	358.3	16925	0.00690
0.17	3.92%	364.0	0.058	0.103	0.009	369.0	9902	0.00404
0.13	2.88%	380.0	0.027	0.103	0.019	380.9	1597	0.00065

## 6 Appendix

Table 6.4: Discrete model values E3

$\dot{F} [\frac{kg}{h}]$	$x_1 [\frac{kg}{kg}]$	$T_{sat} [K]$	$\delta_f [mm]$	$\lambda [\frac{W}{mK}]$	$\dot{m} [Pa s]$	$T_w [K]$	$\dot{q} [\frac{W}{m^2}]$	$\dot{m} [\frac{kg}{m^2 s}]$
3.60	25.49%	298.0	0.382	0.127	0.105	334.7	12308	0.00502
3.32	23.53%	299.6	0.362	0.124	0.098	334.9	12304	0.00502
3.05	21.57%	301.5	0.341	0.122	0.090	335.2	12263	0.00500
2.77	19.61%	303.7	0.318	0.120	0.080	335.4	12196	0.00497
2.49	17.65%	306.4	0.293	0.117	0.070	335.7	12074	0.00492
2.22	15.69%	309.6	0.266	0.115	0.060	336.2	11856	0.00483
1.94	13.73%	313.6	0.237	0.113	0.049	336.9	11496	0.00469
1.66	11.76%	318.6	0.208	0.111	0.039	338.2	10861	0.00443
1.38	9.80%	325.1	0.180	0.109	0.030	340.4	9737	0.00397
1.11	7.84%	333.8	0.153	0.107	0.024	344.2	7754	0.00316
0.83	5.88%	345.8	0.124	0.105	0.017	350.5	4311	0.00176
0.74	5.25%	358.2	0.102	0.105	0.011	358.2	0	0.00000

Table 6.5: Discrete model values E4

$\dot{F} [\frac{kg}{h}]$	$x_1 [\frac{kg}{kg}]$	$T_{sat} [K]$	$\delta_f [mm]$	$\lambda [\frac{W}{mK}]$	$\dot{m} [Pa s]$	$T_w [K]$	$\dot{q} [\frac{W}{m^2}]$	$\dot{m} [\frac{kg}{m^2 s}]$
3.60	31.37%	294.4	0.402	0.135	0.119	352.3	19695	0.00803
3.37	29.41%	295.5	0.388	0.133	0.115	352.4	19732	0.00804
3.15	27.45%	296.6	0.373	0.130	0.111	352.4	19770	0.00806
2.93	25.49%	298.0	0.357	0.127	0.105	352.5	19826	0.00808
2.70	23.53%	299.6	0.338	0.124	0.098	352.4	19918	0.00812
2.48	21.57%	301.5	0.319	0.122	0.090	352.3	20015	0.00816
2.25	19.61%	303.7	0.297	0.120	0.080	352.2	20148	0.00821
2.03	17.65%	306.4	0.273	0.117	0.070	352.1	20271	0.00826
1.80	15.69%	309.6	0.248	0.115	0.060	352.0	20394	0.00831
1.57	13.73%	313.6	0.221	0.113	0.049	352.0	20434	0.00833
1.35	11.76%	318.6	0.194	0.111	0.039	352.5	20234	0.00825
1.12	9.80%	325.1	0.168	0.109	0.030	353.7	19593	0.00799
0.90	7.84%	333.8	0.143	0.107	0.024	356.3	18050	0.00736
0.67	5.88%	345.8	0.124	0.105	0.017	350.5	4311	0.00176
0.60	5.25%	383.2	0.102	0.105	0.011	358.2	0	0.00000

## 6 Appendix

Table 6.6: Overview of different experiments. Chosen settings and results from (Ahmad et al., 2016), (Burkhart, 2016) and results from this thesis. F13 is an unmentioned experiment that was conducted after this thesis was written

Experiment	$F [\frac{kg}{h}]$	$\theta_h [^{\circ}C]$	$p [mbar]$	$\theta_{residueheater} [^{\circ}C]$	$x_{1,F} [\frac{kg}{kg}]$	$x_{1,r} [\frac{kg}{kg}]$
Ahmad8	3.59	78	21	62	80.0%	5.0%
Ahmad9	4.3	77	16	60	80.0%	5.0%
Burkhart9	3.6	85	17.5	80	82.7%	7.7%
Burkhart18	3.6	85	18	80	79.1%	6.9%
E1	3.56	85	14.9	off	81.7%	14.1%
E2	3.57	110	14.7	off	81.5%	11.8%
E3	3.54	85	15	off	26.1%	8.8%
E4	3.52	110	15	off	30.4%	8.6%
F13	3.6	85	20	80	86.8%	11.8%

Table 6.7: Average values of  $\theta_r$  (3 runs per setting) for different run times. The rising residue temperature indicate a possibly varying residue

time	E1	E2	E3	E4
0 min	39.47 °C	55.57 °C	46.37 °C	53.33 °C
10 min	55.43 °C	65.03 °C	65.73 °C	71.60 °C
20 min	60.43 °C	70.63 °C	67.30 °C	80.93 °C
30 min	61.43 °C	73.77 °C	68.77 °C	82.53 °C